CHAPTER TWO

Space-time optics

Davud Hebri[a] **and Sergey A. Ponomarenko**[a,b,*]
[a]Department of Physics and Atmospheric Science, Dalhousie University, Halifax, Nova Scotia, Canada
[b]Department of Electrical and Computer Engineering, Dalhousie University, Halifax, Nova Scotia, Canada
*Corresponding author. e-mail address: serpo@dal.ca

Contents

Abstract

We review recent advances in the emerging field of space-time optics which deals with structured wave packets of light with non-separable (entangled) spatial and temporal degrees of freedom. We first consider space-time light sheets whose electromagnetic fields are uniform in one of the dimensions transverse to their propagation direction. We then proceed to discuss more complex spatiotemporal optical fields with nontrivial topological structures as well as spatiotemporal surface electromagnetic waves. We also review wave packets of random light with structured space-time field correlations. We conclude with a brief discussion of promising applications and offer an outlook of future research and challenges ahead.

Progress in Optics, Volume 71
ISSN 0079-6638, https://doi.org/10.1016/bs.po.2025.07.001

1. Introduction

Optical fields with controllable amplitude, phase, polarization and coherence distributions in space and/or time (frequency) fall into the domain of structured light (Rubinsztein-Dunlop et al., 2016; Forbes, 2019; Forbes et al., 2021; He et al., 2022; Buono & Forbes, 2022; Bliokh et al., 2023; Shen et al., 2023b). Currently, versatile optical beam shaping and spatial coherence modulation techniques (Forbes, 2019; Cai et al., 2017) enable sculpting the spatial degrees of freedom (DoF) of coherent and statistical optical wave packets to generate a garden variety of structured light fields. The most prominent examples include complex Gaussian (Ponomarenko, 2011; Chen et al., 2017; Mao et al., 2019), Hermite-Gaussian (Zauderer, 1986; Wang et al., 2016b; Kotlyar & Kovalev, 2014), Laguerre-Gaussian (Allen et al., 1992a; Yang et al., 2022; Plick & Krenn, 2015), Hermite-Laguerre-Gaussian (Abramochkin & Volostnikov, 1991, 2004; Abramochkin et al., 2010; Abramochkin & Volostnikov, 2010) and Ince-Gaussian (Bandres & Gutiérrez-Vega, 2004) beams, most of which remain shape-invariant on propagation in free space. The propagation-invariant modes, such as Bessel (Durnin, 1987; Khonina et al., 2020; Céspedes Vicente & Caloz, 2021), Airy (Balazs & Berry, 1979; Siviloglou & Christodoulides, 2007; Efremidis et al., 2019), Mathieu (Gutiérrez-Vega et al., 2000), parabolic (Bandres et al., 2004), and Weber (Rodriguez-Lara, 2010) beams, which defy free-space diffraction and exhibit self-healing upon encountering obstacles (Broky et al., 2008), have also been extensively studied to date and their finite-energy realizations have been experimentally demonstrated (Durnin et al., 1987; Siviloglou et al., 2007). At the same time, some of the very same structured light beams can serve as coherent modes (Mandel & Wolf, 1995), or pseudo-modes (Martinez-Herrero et al., 2009; Yang et al., 2015) of random light sources, such as Gaussian-Schell model (Gori, 1980; Starikov & Wolf, 1982), twisted Gaussian Schell model (Sundar et al., 1993; Ponomarenko, 2001b), Bessel-correlated (Gori et al., 1987), and modified-Bessel-correlated (Ponomarenko, 2001a) sources to name but a few representative examples. Instructively, nearly incoherent beams manifest robust self-healing capabilities regardless of their spatial intensity distribution and coherence structure (Wang et al., 2012; Xu et al., 2020). Moreover, partially coherent diffraction free beams can also be engineered (Ponomarenko et al., 2007; Hajati et al., 2021; Cao et al., 2025) by tailoring correlations among propagation-invariant coherent modes.

The spatial DoFs of light fields have been the primary focus within the realm of diffractive optics. In this context, temporal optical DoFs can be ignored by treating light fields as either coherent, monochromatic beams, or quasi-monochromatic, statistically stationary fields of very narrow bandwidth. Meanwhile, recent advances in ultrafast optics have helped researchers gain unprecedented control of the temporal DoFs of ultrashort optical pulses (Weiner, 2011; Jiang et al., 2007; Cundiff & Weiner, 2010). Yet, the separable spatial DoFs of such pulsed fields are typically assumed trivial, corresponding to either uniform plane waves, or optical fiber modes.

Until recently, diffractive and ultrafast optics have largely developed independently, with minimal overlap between the respective research communities. However, the momentous advances in generating propagation-invariant optical waves, localized in both space and time, in free space (Saari & Reivelt, 1997; Kondakci & Abouraddy, 2017), linear (Porras et al., 2003; Porras & Di Trapani, 2004; Chong et al., 2010) and nonlinear (Conti et al., 2003) media have triggered accelerating interest in spatiotemporal wave packets (STWP) of light with non-separable spatial and temporal DoFs that can be tailored on demand. Exploring structured space-time light packets and topologically nontrivial states of light, such as spatiotemporal optical vortices, skyrmions, hopfions, knots and links, establishes a gateway into the fundamental behavior of analogous fields in more complex and far less experimentally accessible settings in condensed matter physics, classical and quantum field theory and gravity (Baez & Muniain, 1994). In addition, customizable optical STWPs can open the door to a host of promising applications in robust optical communications, ultrafast optical computing, precise optical imaging and microscopy, reliable microparticle guiding and trapping and secure quantum information processing, among others (Liu et al., 2024a).

Here we review the salient features of STWPs, stressing the fundamental aspects, such as their topological structure, on propagation in free space or dispersive media, as well as any new physics that arises from space-time non-separability. We only briefly mention any protocols for the laboratory realization of STWPs and only at a conceptual level. We refer the reader interested in STWP generation and techniques for their spatiotemporal characterization in greater detail to several excellent reviews (Yessenov et al., 2022b; Wan et al., 2023; Bekshaev, 2024; Zhan, 2024; Liu et al., 2024a); see also (Yessenov et al., 2022b) for a comprehensive review of historic development of the subject of spatiotemporal wave packet dynamics.

In the next section, we review the physics of space-time light sheets in free space or linear media with no frequency dispersion, followed by the discussion of more complex coherent STWPs with nontrivial topological structures in the third section. The fourth section is devoted to structured random STWPs and wave packets of random surface plasmon polaritons. Finally, we briefly speculate on promising applications of STWPs and outline directions for future research on the subject.

2. Space-time light sheets

We can design any space-time wave packet by employing a tailored superposition of elementary modes of variable degree of structural complexity. The simplest such mode is a plane wave. The angular spectrum representation provides a universal and physically intuitive picture of STWPs composed of plane waves. In this section, we present a unified angular spectrum picture of space-time light sheets that are uniform in one of the two orthogonal directions transverse to their propagation direction.

2.1 Angular spectrum representation of space-time light sheets

The electric field $\mathbf{E}$ of a wave packet propagating in free space is governed by the wave equation

$$\nabla^2\mathbf{E} - c^{-2}\partial_{tt}^2\mathbf{E} = 0. \tag{1}$$

Assuming a linearly polarized electric field of the wave packet, which propagates in the z-direction, is uniform in the y-direction, say, we can express $\mathbf{E}$ in terms of an envelope $\Psi(x, t, z)$ and a carrier as

$$\mathbf{E}(\mathbf{r}, t) = \mathbf{e}_y\Psi(x, t)\, e^{i(k_0 z-\omega_0 t)}. \tag{2}$$

Here ω_0 and $k_0 = \omega_0/c$ are the frequency and wave number of the carrier wave; further, $\mathbf{e}_y$ is a unit polarization vector. Such an STWP is known as a space-time (ST) light sheet. Assuming unidirectional propagation of the ST light sheet from a source at $z = 0$ into a positive half-space $z \geq 0$, we can express the field envelope in terms of its angular spectrum as

$$\Psi(x, t, z) = \int d\Omega \int dk_x\, \mathcal{A}(k_x, \Omega)\, e^{ik_x x} e^{iq_z z} e^{-i\Omega t}, \tag{3}$$

where $\Omega = \omega - \omega_0$ and $q_z = k_z - k_0$ and we introduced an angular spectrum amplitude $\mathcal{A}(k_x, \Omega)$. In free space, each monochromatic component of the angular spectrum obeys the dispersion relation

$$k_x^2 + k_z^2 = \omega^2/c^2. \tag{4}$$

The dispersion relation furnishes a very simple and intuitive geometric picture of any light sheet. According to Eq. (4), all plane waves comprising the angular spectrum of the wave packet lie on a surface of a light cone, with the axis of the temporal frequency ω coinciding with the cone axis. In this picture, any monochromatic beam or a plane wave pulse can be geometrically represented by a section of the cone with a plane, either $\omega = \omega_0$, or $k_x = 0$, respectively, as is shown in Fig. 1A and B. For a monochromatic beam, spectral projections onto the $(k_z, \omega/c)$ and $(k_x, \omega/c)$ planes are straight lines and that onto the (k_x, k_z)-plane a semicircle after excluding $k_z < 0$. For a plane-wave pulse, a spectral projection onto any plane is a straight line. Further, a conventional pulsed beam with separable spatial and temporal DoFs corresponds to a 2D patch on the surface of the cone, see Fig. 1C. At the same time, a spatiotemporal wave packet of light involves tightly coupled spatial and temporal DoFs and hence it must be represented by a curve on the light cone. Mathematically, this constraint can be expressed by either assuming a tight one-to-one coupling between individual spatial and temporal frequencies within the STWP bandwidth, or, more generally, the angular spectrum non-separability as a function of k_x and ω. In this section, we assume that the first situation is realized, so that

$$\mathcal{A}(k_x, \Omega) = \mathcal{A}(k_x)\delta[\Omega - \Omega(k_x)], \tag{5}$$

where $\delta(\ldots)$ is a Dirac delta-function. Thus, a number of possible STWPs can be generated by customizing coupling between spatial and temporal

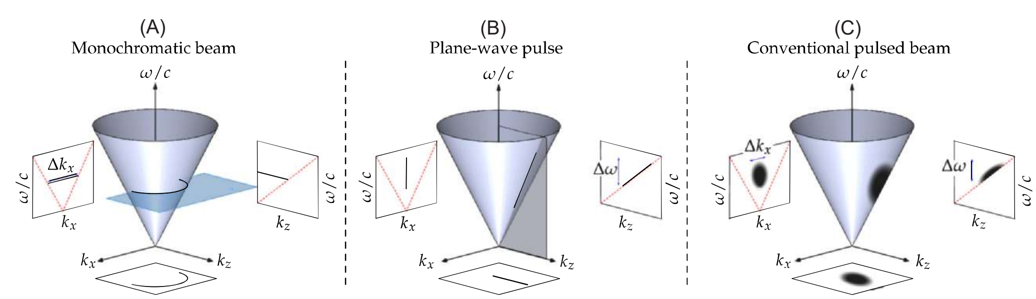

Fig. 1 Spectral support domain on the light-cone surface for (A) monochromatic beam, (B) plane-wave pulse and (C) conventional (separable) pulsed beam.

frequencies of the angular spectrum of a light source. Therefore, the angular spectrum representation of STWPs is most germane to their laboratory realization that invariably involves angular spectrum engineering at the source (Yessenov et al., 2022b; Zhan, 2024).

2.2 Propagation-invariant and accelerating space-time light sheets

The vast majority of work on space-time light sheets to date has been concerned with propagation-invariant STWPs that defy free-space diffraction. The propagation-invariant STWPs can be generated by imposing the following phase-space coupling (Kondakci & Abouraddy, 2017):

$$q_z = (\Omega/c)\cot\theta, \tag{6}$$

where the control parameter θ has the geometrical meaning of the tilt angle the plane specified by Eq. (6) makes with the q_z axis in the Fourier space. The angular spectrum support of each propagation-invariant STWP is a conical section—hyperbola, parabola, ellipse, circle, or a pair of lines—obtained by the intersection between the tilted plane and the light cone. It follows at once from Eqs. (3), (5) and (6) that the field envelope at the source $\Psi_0(x, t) = \Psi(x, t, z = 0)$ is rigidly transported in the axial direction,

$$\Psi(x, t, z) = \Psi_0(x, t - z/\tilde{v}), \tag{7}$$

with the group velocity given by the expression

$$\tilde{v} = c\tan\theta = c/\tilde{n}. \tag{8}$$

Here we also introduced an (adjustable) effective group index, $\tilde{n} = \cot\theta$, which has proven useful in the studies of the behavior of propagation-invariant STWPs at an interface separating two dispersionless media. Depending on the magnitude of the group index, such STWPs can be subluminal, $(0 < \theta \leq 45°)$, superluminal, $(45° \leq \theta < 90°)$, or even backward propagating with a negative group velocity in the parameter regime $90° < \theta < 180°$.

The propagation-invariant light sheets were realized in the laboratory in a widely tunable range of group velocities from −4c to 30c in pioneering experiments (Kondakci & Abouraddy, 2017, 2019). We sketch the corresponding experimental protocol in Fig. 2. The ST light sheet generation in a laboratory involves three steps. The first step is a high-resolution spectral analysis in which a well-collimated plane-wave pulse from the source is resolved with a diffraction grating G_1 in the (uniform) y-direction, followed by collimating a spectrally resolved wave front with a cylindrical lens CL_1. At this stage, each temporal frequency is assigned to a given column in the y-direction. The resulting pulse then enters an SLM that works in transmission or reflection mode. Next, the spectrally resolved wave front is spatially modulated by the SLM in the $x-$ direction, thus realizing tight coupling between pairs of spatial and temporal frequencies via the 2D modulation in the SLM plane. Finally, the sculpted angular spectrum of the pulse is sent to an identical pair of cylindrical lens and grating, CL_2 and G_2, see Fig. 2, if working in the SLM transmission mode, or retro-reflected otherwise to reconstitute an STWP in the form of a light sheet.

We exhibit experimental results in Fig. 3. We observe in the figure that an STWP of width (FWHM) 14 μm can propagate a distance of around 100 mm without any noticeable distortion of its central part. By comparison, this distance corresponds to roughly 140 Rayleigh ranges of a Gaussian beam of the same FWHM. As the spatial width of the light sheet is reduced, so does its diffraction free propagation distance: An STWP of 7 μm width propagates for about 25 mm until the diffraction starts taking its toll. Further, the superimposed yellow curve in Fig. 3 is the axial evolution of the central-peak power of the pulse. We observe that regardless of the source beam width, the central peak power of the pulse is approximately conserved as well.

Alternatively, we can interpret the propagation invariance of a paraxial light sheet in terms of a time diffraction concept (Moshinsky, 1952; Longhi, 2004; Porras, 2017; Bliokh & Nori, 2012). According to Eqs. (3), (5) and (6) in the paraxial approximation, $k_x \ll k_0$, we can rewrite the field envelope of such a propagation-invariant sheet as

$$\Psi(x, t, z) = \int dk_x\, \mathcal{A}(k_x)\exp(ik_x x)\exp\left[-\frac{ik_x^2(t - z/\tilde{v})}{2k_0(c^{-1} - \tilde{v}^{-1})}\right]. \tag{9}$$

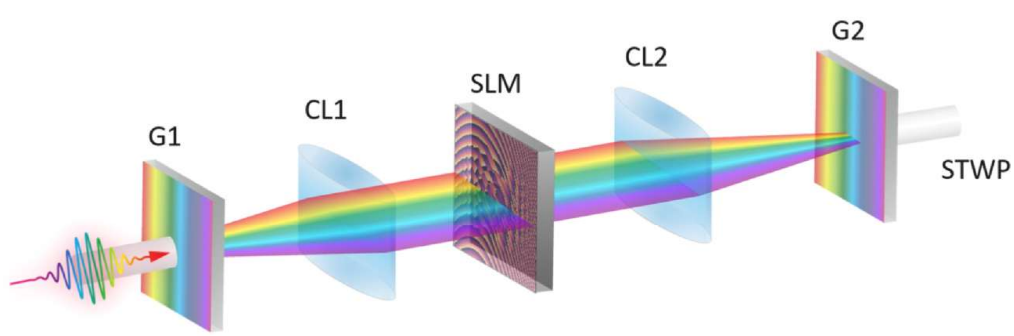

Fig. 2 Illustrating space-time light sheet synthesis: A conceptual sketch. G_1 and G_2: two identical gratings for spectral resolution and synthesis; CL_1 and CL_2: two identical cylindrical lenses; SLM: spatial light modulator realizing 2D wavefront modulation in its plane.

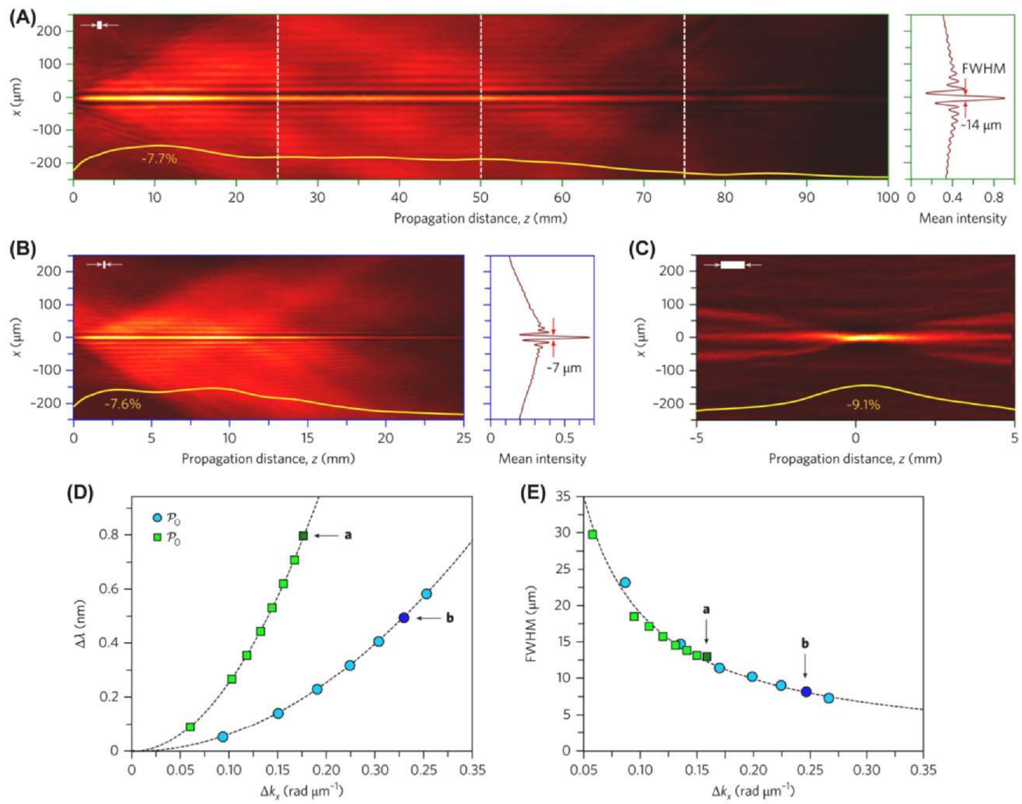

Fig. 3 Propagation of diffraction-free ST light sheets. (A) Measured spatial distribution of intensity $I(x, z)$ of the field. Right panel: Axially averaged intensity over 100 mm. (B) Measured $I(x, z)$ which produces a $\Delta x \approx 7\ \mu$m central feature preserved for 25 mm. (C) Measured $I(x, z)$ which produces a 16.4 μm central feature preserved for 750 μm. The solid white lines in the top-left corners of a-c are the Rayleigh ranges $z_R = 555$, 136, 750 μm for Gaussian beams with the widths 14, 7 and 16.4 μm, respectively. (D) Measured relationship between $\Delta\lambda$ and Δk_x for ST light sheets. Dashed lines are parabolic fits for the paraxial limit. (E) Measured dependence of Δx on Δk_x. *F(E) From Kondakci and Abouraddy (2017).*

Eq. (9) is analogous to the Fresnel evolution of a monochromatic beam in free space with the identification $z \to (t - z/\tilde{v})/(c^{-1} - \tilde{v}^{-1})$. Thus, the spatiotemporal field envelope Ψ at any $z = const$ is closely related to the diffraction pattern of a monochromatic beam of the same spatial bandwidth. In other words, STWP diffraction in the transverse plane occurs at different rates for different time slices, thereby ensuring the invariance of its overall spatiotemporal profile.

Ideal space-time light sheets carry infinite energy and can defy diffraction ad infinitum. However, the propagation distance over which realistic space-time light sheets can resist diffraction is determined by the fact that a given spatial frequency can only be coupled to a narrow range of temporal frequencies. The width of this range, which is finite due to the finite spectral resolution of any realistic experimental setup for generating STWPs, is known as spectral uncertainty. The latter determines both the energy content and diffraction-free propagation distance of space-time light sheets in the laboratory. If we replace a delta function in Eq. (5) with a finite envelope, we can estimate the propagation distance in terms of the spectral uncertainty as (Yessenov et al., 2019b)

$$L_{\max} \simeq \frac{c}{\delta\omega}\frac{1}{|1-\cot\theta|}, \tag{10}$$

where $\delta\omega$ is the spectral uncertainty. The distances as long as 70 m are attainable through optimizing $\delta\omega$ and θ (Bhaduri et al., 2019).

Furthermore, the spectral uncertainty ensures causality is not violated regardless of the value of $\tilde{v}$. Indeed, the analysis reveals (Yessenov et al., 2019b) that the envelope of any finite-energy STWP is a product of a broad pilot wave, which carries the STWP energy and propagates with the speed of light, and an ideal STWP envelope. It follows that the envelope of an ideal subluminal STWP lags behind the pilot wave and at some distance, the former is overtaken by the trailing edge of the latter. For a superluminal or backward propagating STWP, the ideal envelope eventually catches up to the leading edge of the pilot wave. We sketch these scenarios in Fig. 4 where we represent the pilot as a red rectangular box and the ideal STWP as a blue bell-like shape. This pilot+envelope structure of a propagation-invariant STWP guarantees that no information can be carried away from the source to a receiver faster than the speed of light. The distance over which the ideal envelope "collides" with the pilot wave sets the limit beyond which the laboratory-generated STWP quickly succumbs to diffraction.

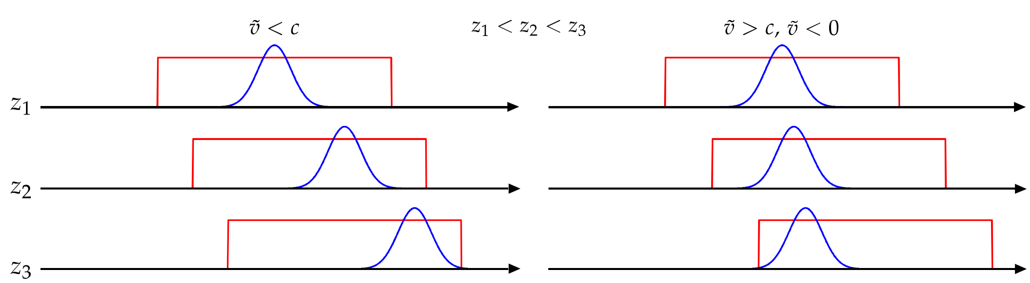

Fig. 4 Illustrating the structure of a realistic finite-energy STWP that ensures at no point causality is violated. The snap-shots of the STWP profile are taken at three progressively increasing propagation distances $z_1 < z_2 < z_3$.

In addition to propagation-invariant light sheets, accelerating STWPs can also be engineered. The idea behind this design lies in considering a 2D spectral support domain between the 1D conical sections corresponding to two propagation-invariant STWPs associated with different (initial and final) tilt angles θ_i and θ_f. It stands to reason to conjecture that this domain describes accelerating space-time light sheets with group velocities in the range $\tilde{v}_i \leq \tilde{v} \leq \tilde{v}_f$, where $\tilde{v}_i = c\tan\theta_i$ and $\tilde{v}_f = c\tan\theta_f$. This hypothesis was tested in a series of experiments (Yessenov & Abouraddy, 2020; Hall et al., 2022) where an axial group velocity profile $v(\tilde{z}) = \tilde{v}_i + v_f(z/L)^m$ of an STWP was designed over a propagation distance L from the source at $z = 0$. Here m is any non-negative real constant. The STWP acceleration is then $a(z) = d\tilde{v}/dz = (mv_f/L)(z/L)^{m-1}$. This way, space-time light sheets traveling with constant (Yessenov & Abouraddy, 2020) ($m = 1$) and controllable (Hall et al., 2022) ($m \neq 1$) acceleration were generated. A complementary approach to sculpting accelerating STWPs with arbitrary axial profiles involves tailoring angular dispersion of space-time light sheets (Li & Kawanaka, 2020a,b; Li et al., 2021).

2.3 Refraction of space-time light sheets at planar interfaces

Novel physical effects arise upon refraction of propagation-invariant light sheets from a planar interface separating two homogeneous, isotropic non-dispersive media (Bhaduri et al., 2020; Allende Motz et al., 2021; Yessenov et al., 2021a). We first consider the case of normal incidence whereby the STWP propagation direction z is along the normal to the interface. In this situation, the energy-momentum conservation at a single photon level implies the continuity of Ω and k_x across the interface. Combining these two conditions with Eq. (6) as well as the dispersion relation, (4) in the paraxial approximation yields the following analogue of a Fresnel refraction law for STWPs (Yessenov et al., 2021b)

$$n_1(n_1 - \tilde{n}_1) = n_2(n_2 - \tilde{n}_2), \tag{11}$$

where n_1 and n_2 are refractive indices of the two media, while $\tilde{n}_1 = \cot\theta_1$ and $\tilde{n}_2 = \cot\theta_2$ are effective group indices, c.f., Eq. (8), associated with the corresponding tilt angles. Eq. (11) is schematically illustrated in Fig. 5.

We can draw several noteworthy conclusions from Eq. (11) and Fig. 5. First of all, the propagation-invariant light sheets remain so upon crossing from the first to the second medium. Second, there are two intriguing particular cases for the effective group velocity change. It turns out that selecting $\tilde{n}_1 = n_1 + n_2$ leads to $\tilde{n}_1 = \tilde{n}_2$, implying the same group velocity in

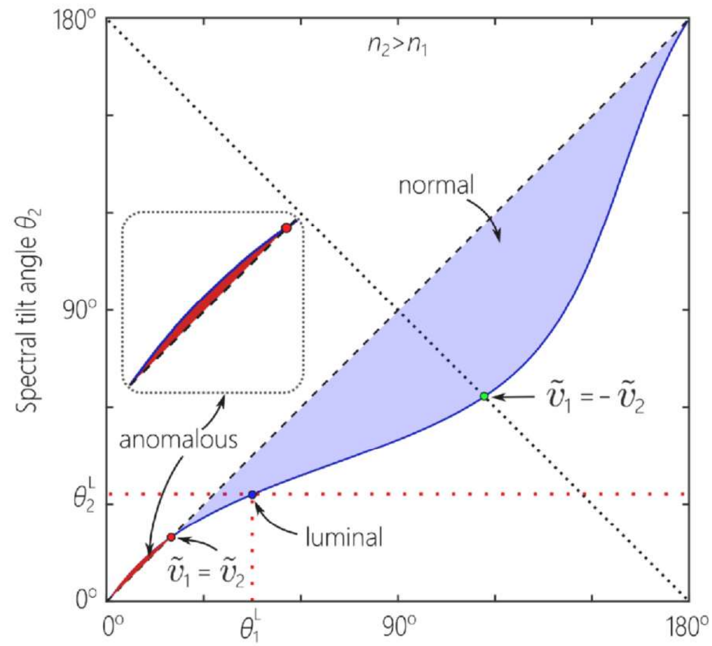

Fig. 5 Illustrating the generic refraction law of Eq. (11) for space-time wave packets at an interface separating any two dielectrics. The inset highlights the anomalous refraction regime. In this example, $n_1 = 1$ and $n_2 = 1.5$. *Reproduced with permission from Yessenov et al. (2021b) ©Optica Publishing Group.*

both media. On the other hand, the choice $\tilde{n}_1 = n_1 - n_2$ results in $\tilde{n}_2 = -\tilde{n}_1$. Therefore, the STWP group velocity reverses its sign in this case. This inversion is illustrated in Fig Fig 5. It readily follows that an STWP traversing identical slabs of the media with indices n_1 and n_2 will incur no group delay at all. Such group-velocity inversion and group delay cancellation were confirmed experimentally (Bhaduri et al., 2020; Allende Motz et al., 2021).

Another instructive feature of propagation-invariant STWP refraction at an interface is related to our ability to adjust the type of STWP refraction by controlling the spectral tilt angle in the medium of incidence. Indeed, by sweeping $\tilde{n}_1$ from below a certain critical value $\tilde{n}_{\text{th}}$, $\tilde{n}_1 < \tilde{n}_{\text{th}}$, to that above the threshold, $\tilde{n}_1 > \tilde{n}_{\text{th}}$, the STWP refraction transitions from normal to anomalous. In the first instance, $\tilde{n}_1 < \tilde{n}_2$ whenever $n_1 < n_2$, which is similar to a refraction of a conventional plane wave pulse in the absence of dispersion: The smaller the refractive index, the greater the group velocity, $v_g = c/n$. Above the threshold, however, the opposite scenario unfolds: $n_1 < n_2$ implies $\tilde{n}_1 > \tilde{n}_2$, which we refer to as anomalous refraction.

Yet, oblique incidence adds a new twist. Although the transmitted STWP is no longer propagation-invariant because the transverse and axial components of the wave vector get mixed, the effective group index $\tilde{n}_2$ depends on the incidence angle for a fixed $\tilde{n}_1$. There are two profound consequences of this dependence. First, there exist so-called isochronous STWPs such that the group delay accrued upon the STWP traversing a non-dispersive medium slab is independent of the incidence angle; the existence of such space-time light sheets was experimentally verified in (Yessenov et al., 2021a). Second, using the dependence of $\tilde{n}_2$ on the angle of incidence, blind synchronization of spatially separated receiver clocks, embedded in the medium with refractive index n_2, was realized (Yessenov et al., 2021a). To this end, a propagation-invariant light sheet, generated in the medium with refractive index n_1, is transmitted into the receiver host medium and the spectral tilt angle θ_1 is adjusted to ensure identical time delay for all monochromatic components of the source reaching all receiver clocks.

2.4 Space-time Talbot effect in free space

Designing spatiotemporal light sheets with discrete angular spectra at the source shines new light on such a fundamental phenomenon as wave packet revivals. In the optical context, wave packet revivals arise as longitudinal revivals of spatially periodic, monochromatic wave packets in the plane transverse to their propagation direction (Patorski, 1989; Wen et al., 2013). The revivals occur periodically with a period known as the Talbot length, $z_T^{(x)} = 2L^2/\lambda_0$, where L is a transverse spatial period of the field and λ_0 is the wavelength of light (Montgomery, 1967; Berry & Klein, 1996). This phenomenon is known as the Talbot effect in honor of Henry Fox Talbot who discovered such periodic revivals past a diffraction grating illuminated with a monochromatic paraxial beam (Talbot, 1836). Interestingly, spatial revivals can also be observed even for an optical field of finite bandwidth (Packross et al., 1984; Lancis et al., 1995; Guérineau et al., 2000).

To visualize the conventional Talbot effect we display in Fig. 6A and B the axial evolution of a monochromatic beam with a continuous angular spectrum and that of the beam with a discrete spectrum exhibited on the corresponding light cone. We can clearly detect spatial Talbot revivals in the latter case. The spatial Talbot effect can also occur for space-time light sheets with a periodically discretized in spatial frequency angular spectrum; such a discretization can be imposed by transmitting propagation-invariant light sheets through a diffraction grating. The experiments reveal an unexpected feature of such spatial Talbot revivals of STWPs (Yessenov et al., 2020). The spatial Talbot effect is observed by monitoring the STWP

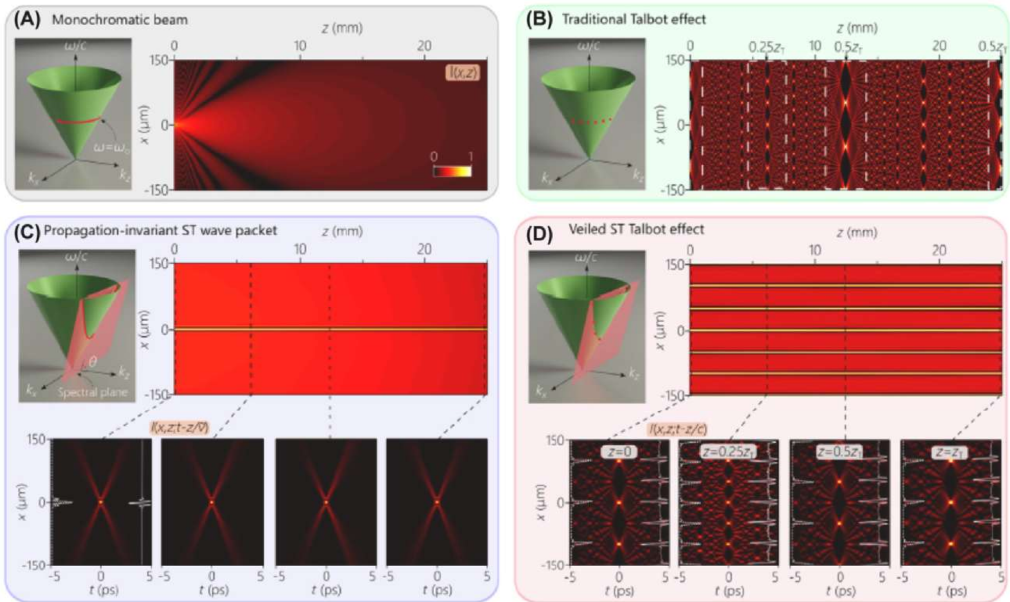

Fig. 6 Concept of the veiled Talbot effect. (A) The evolution of a monochromatic beam with a continuous angular spectrum. (B) The field evolution of monochromatic beam with a discretized angular spectrum (C) The evolution of a propagation-invariant STWP (D) Same as (C) except that the spatial spectrum is sampled at integer multiples of $2\pi/L$ where L is a period of diffraction grating. Copyright (2020) by the American Physical Society. *(D) Reprinted with permission from Yessenov et al. (2020).*

evolution in time as is seen by comparing Fig. 6C and D. The lower panels show spatiotemporal profiles of a propagation-invariant STWP with a continuous angular spectrum in a reference frame moving at $\tilde{v}$ and revivals of an STWP endowed with a discrete spectrum in the reference frame moving at c. However, time-integrated measurements detect no spatial revivals. Rather, they simply yield a propagation-invariant spatial profile of the STWP. Thus, the spatial Talbot effect with STWPs is veiled within their space-time structure as is shown in Fig. 6D.

To observe a temporal analogue of the Talbot effect for a periodic train of pulses propagating in a medium, the latter must be dispersive. Temporal Talbot revivals have been observed to occur in optical fibers over multiple integers of the temporal Talbot length $z_T^{(t)} = T_p^2/(\pi|\beta_2|)$, T_p being a pulse width and β_2 a group-velocity dispersion (GVD) coefficient (Jannson & Jannson, 1981; Azaña & Muriel, 1999). Typically, the observed temporal Talbot lengths are a few kilometers in single-mode fibers. As GVD is, as a rule, a weak effect in bulk dispersive media far away from any internal resonances, temporal Talbot revivals are yet to be observed in the bulk where the much stronger diffraction effects thwart successful measurements.

However, the temporal Talbot effect has been observed with STWPs in free space over a few-centimeter long propagation distances (Hall et al., 2021a). To this end, the angular spectrum of STWP was sculpted to impose the correlations between spatial and temporal frequencies of the form $q_z = \Omega/\tilde{v} + \beta_2\Omega^2/2$. The latter is identical to the dispersion relation for any monochromatic component of a pulse propagating with group velocity $\tilde{v}$ in a medium with the GVD coefficient β_2. Therefore, the STWP field on the axis, $x = 0$ will undergo periodic Talbot revivals. Notice that the effective dispersion is triggered in free space due to space-time coupling of the light source. This approach was implemented in the experiment (Hall et al., 2021a). The first temporal Talbot revivals were observed with either normal or anomalous effective GVD over the Talbot distance of around 20 mm in free space.

The spatial and temporal Talbot effects with conventional, separable in space and time, wave packets occur over vastly different length scales. While the spatial revivals typically unfold over a few millimeters or centimeters, depending on the period of diffraction grating, the temporal ones usually require kilometers of a fiber. Thus, a simultaneous spatiotemporal revival can only occur under very fortuitous circumstances of commensurable spatial and temporal Talbot lengths, $z_T^{(t)} = Nz_T^{(x)}$, with $N \gg 1$ being a very large integer. For this reason, simultaneous space-time revivals of conventional pulsed beams with separable spatiotemporal DoFs have never been observed in the laboratory.

At the same time, a space-time Talbot effect can be realized with judiciously tailored STWPs. To see how this feat can be accomplished, let us consider the following space-time spectral correlations:

$$\Omega/c = \alpha k_x, \tag{12}$$

where α is a dimensionless coupling constant. In the paraxial approximation, the dispersion relation (5) can be cast into the form

$$q_z = \frac{\Omega}{c} - \frac{k_x^2}{2k_0}. \tag{13}$$

On eliminating either $\boldsymbol{\Omega}$ or k_x from Eq. (13) with the help of (12), we obtain

$$q_z = \alpha k_x - \frac{k_x^2}{2k_0} = \frac{\Omega}{c} - \frac{|\beta_2|}{2}\Omega^2, \tag{14}$$

where the effective GVD coefficient reads $\beta_2 = -k_0^{-1}(\alpha c)^{-2}$. It follows from Eq. (14) that since spatial and temporal frequencies obey the same dispersion relation, spatial diffraction and temporal dispersion of thus sculpted STWs unfold in lock step. Spatial discretization of such an STWP with a period L triggers its temporal discretization with a period $T = L/(\alpha c)$ due to the angular spectrum correlations expressed in Eq. (12). Therefore, such wave packets undergo simultaneous spatial and temporal revivals over multiples of the same Talbot length $z_T = 2L^2/\lambda_0 = T^2/(\pi|\beta_2|)$, thereby realizing a space-time Talbot effect.

This conjecture was tested experimentally in (Hall et al., 2021b) where the space-time Talbot effect was observed over a distance of a few centimeters, see Fig. 7. We can infer from the figure that despite dramatic differences between the evolution of the field in (C) and (D), their

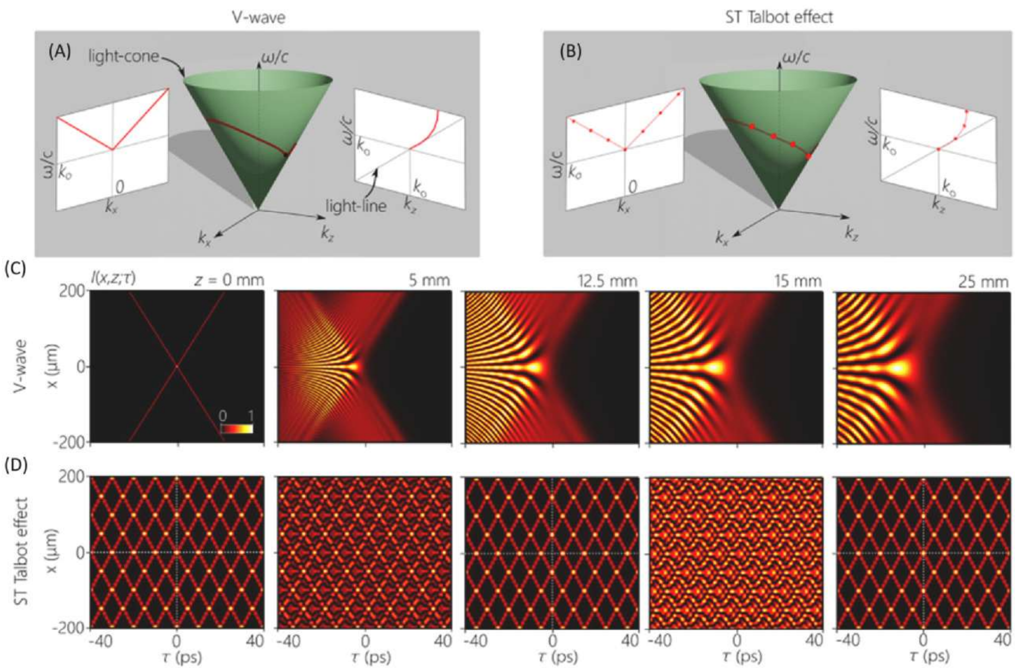

Fig. 7 Concept of the space-time Talbot effect. (A) Representation of the spectral support domain of a V-wave with a continuous angular spectrum on the surface of the light-cone and its spectral projections onto the (k_x, ω/c) and (k_z, ω/c) planes. (B) The space-time Talbot effect is realized by discretizing the spatiotemporal spectrum of the V-wave in (A). (C) Spatiotemporal profiles $I(x, z; \tau)$ of a V-wave propagating in free space in a reference frame moving at c and experiencing GVD. (D) Spatiotemporal intensity profiles $I(x, z; \tau)$ corresponding to the spatiotemporal spectrum shown in (B) and demonstrating the space-time Talbot effect. The white dotted lines are guides for the eye and highlight the half-period shift in space and time at the mid-Talbot plane ($z = 0.5z_T$) with respect to the full-Talbot planes ($z = 0$ and $z = z_T$). *(D) From Hall et al. (2021b).*

spatiotemporal spectra are identical except for the discretization of the latter. In the experiment, a slightly different angular spectrum correlations were imposed, $\Omega = \alpha c|k_x|$ for convenience of working with positive frequencies, $\Omega > 0$. Due to a characteristic V shape of their angular spectrum correlations, the customized STWPs that experience space-time Talbot revivals were dubbed "V-waves" [Hall et al. (2021b); Hall and Abouraddy (2021). Lately a $3D$ version of the space-time Talbot effect has been discussed theoretically by assuming a coupling $\Omega/c = \sqrt{k_x^2 + k_y^2}$ (Zhang et al., 2025).

We stress that the discussed spatial, temporal and spatiotemporal Talbot revivals of STWPs emerge as a result of the angular spectrum discretization of space-time correlated paraxial sources in free space. These effects should not be confused with self-imaging of paraxial wave packets with continuous angular spectra (Saari & Reivelt, 1997), or that brought about by self-lensing properties of graded-index media (Ponomarenko, 2015; Agrawal, 2023).

2.5 Spatiotemporal wave packets localized in three dimensions

To this point, we have been considering space-time light sheets uniform in one of the two orthogonal directions in the transverse plane of the STWP field. One uniform spatial dimension is required to arrange and label spectrally resolved temporal frequencies within the source bandwidth along this spare dimension for subsequent coupling with spatial frequencies in the orthogonal dimension on an SLM, say. This strategy can be extended to sculpt axially symmetric STWPs with all three DoFs—two transverse spatial and one axial temporal—correlated (Yessenov et al., 2022a). This can be accomplished by noticing that the 3D dispersion relation of light in free space in Cartesian coordinates reads

$$k_x^2 + k_y^2 + k_z^2 = \omega^2/c^2. \tag{15}$$

For axially symmetric STWPs, Eq. (15) can be rewritten in cylindrical coordinates as

$$k_r^2 + k_z^2 = \omega^2/c^2, \tag{16}$$

where k_r is a radial wave number. Imposing the angular dispersion of Eq. (6), we can obtain a 3D propagation-invariant paraxial wave packet of spatio-temporal profile as

$$\Psi(r, z, t) = \Psi(r, 0, t - z/\tilde{v}), \tag{17}$$

where the spatio-temporal profile at the source can be expressed in terms of the angular spectrum $\mathcal{A}(k_r)$ as

$$\Psi(r, 0, t) = \int dk_r k_r \mathcal{A}(k_r) J_0(k_r r) e^{-i\Omega(k_r)t}. \tag{18}$$

Here $J_0(x)$ is a Bessel function of order zero and $\tilde{v} = c\tan\theta$ is a group velocity corresponding to the spectral tilt angle θ.

The spectral support of these axially symmetric, propagation-invariant 3D STWPs in $(k_r, k_z, \omega/c)$-space is a conical section obtained by the intersection of a plane $q_z = (\Omega/c)\cot\theta$ with a light cone, just as is the case of the previously discussed propagation-invariant light sheets. However, to appreciate the role of an additional dimension, we must also consider a complementary $(k_x, k_y, \omega/c)$-space picture of the STWP. In Fig. 8A, we display the spectral support domain of a superluminal 3D space-time wave packet at the intersection of the light cone $k_r^2 + k_z^2 = (\omega/c)^2$ with a spectral plane that is parallel to the k_r-axis, making an angle $\theta > 45°$ with the k_z-axis. The conic section at the intersection is a hyperbola. In $(k_x, k_y, \omega/c)$-space, the spectrum is half of a two-sheet elliptic hyperboloid (only the upper sheet is displayed in the figure). By the same token, the subluminal STWPs ($\theta < 45°$) have an elliptic spectral domain support on the light cone and are represented in $(k_x, k_y, \omega/c)$-space by prolate or oblate spheroids, as is seen in Fig. 8B. Crucially, the wavelengths of the projection of a superluminal (subluminal) STWP onto the (k_x, k_y)-plane are arranged in concentric circles of decreasing (increasing) radius with the wavelength. We note that each such wave packet has a hyperboloid-like spatiotemporal intensity profile with an X-wavelike cross section in any spatiotemporal plane transverse to the propagation direction z.

Conceptually, the experimental protocol to generate such 3D STWP involves three stages, which we sketch in Fig. 9. The idea is to start with a generic plane-wave pulse and realize an angular-dispersion synthesizer in two dimensions that arranges the wavelengths in circles in a prescribed order: S_1 corresponds to a subluminal wave packet, whereas S_2 and S_3 correspond to superluminal wave packets of different group velocities (Fig. 9A). At the first stage, a collimated plane-wave pulse is spectrally analyzed by spatially separating temporal frequencies of the pulse in one of the two orthogonal transverse directions as was done with space-time light sheets. Next, the spectral components undergo a tunable 1D spectral transformation that rearranges the initial wavelength sequence into a spectrally resolved wave front. At the last stage, a 2D Cartesian-to-log-

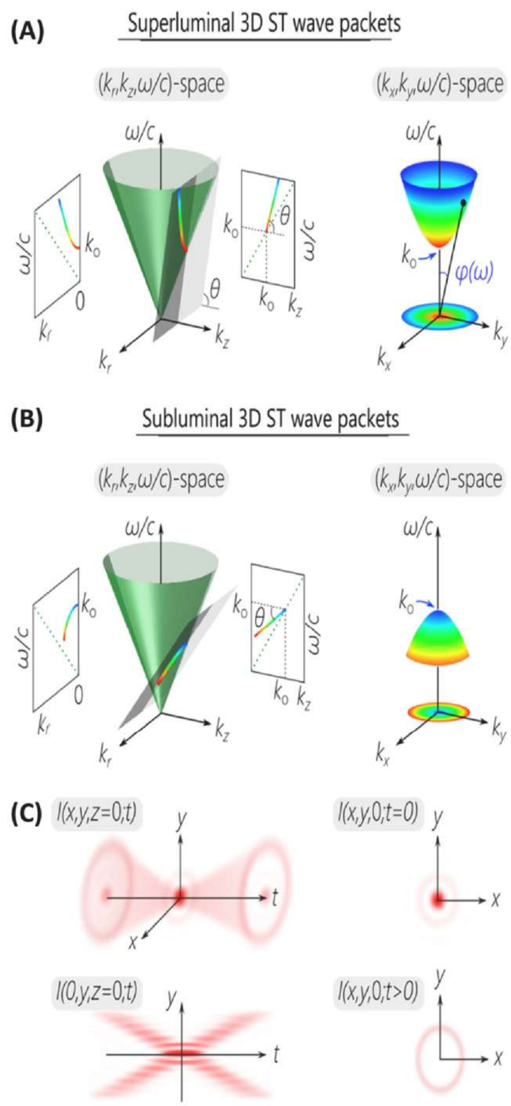

Fig. 8 Visualization of the spectral support domain for 3D space-time wave packets on the surface of the free-space light cone. The spectral support domain for a (A) superluminal and (B) subluminal 3D space-time wave packet. (C) Spatiotemporal intensity profile $I(x, y, z = 0; t)$ at a fixed axial plane $z = 0$, the intensity profile in a meridional plane $I(0, y, z = 0; t)$, and the transverse profiles at the wave-packet center $I(x, y, 0; 0)$ and off-center $I(x, y, 0; t > 0)$. *(C) From Yessenov et al. (2022a).*

polar conformal transformation is applied to convert vertical spectral lines into concentric circles in the $k-$space. This transformation was originally introduced a while ago (Bryngdahl, 1974; Hossack et al., 1987) and has been recently implemented as a methodology for orbital angular momentum sorting (Berkhout et al., 2010; Lavery et al., 2012) and the generation of toroidal vortices of light (Wan et al., 2022a) which we discuss in the next section.

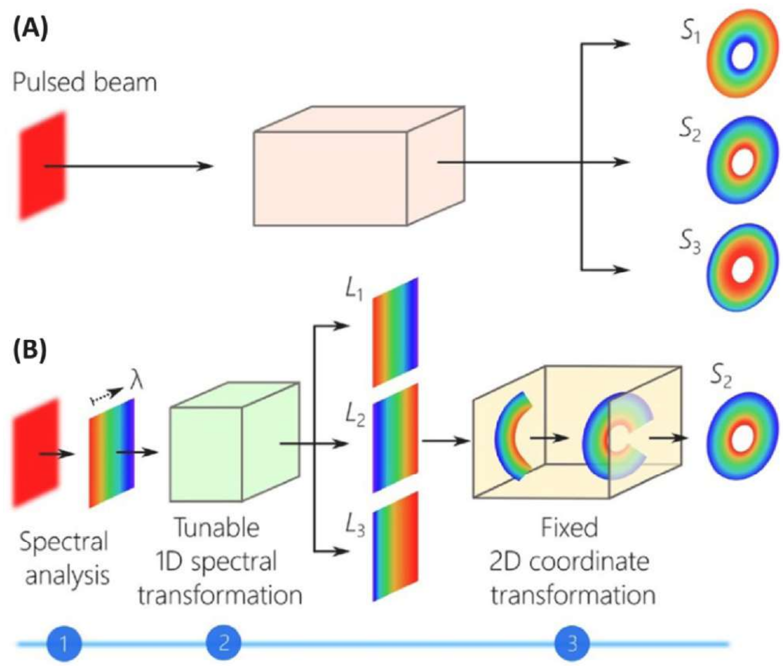

Fig. 9 Synthesis strategy for 3D ST wave packets. (A) Starting with a generic plane-wave pulse arrange the wavelengths in circles in a prescribed order. (B) Spectral analysis followed by a tunable 1D spectral transformation that rearranges the initial wavelength sequence in the spectrally resolved wavefront. The 1D spectra L_1, L_2, and L_3 are rectilinear counterparts of S_1, S_2, and S_3 in a. In the third stage, a fixed 2D conformal coordinate transformation converts vertical lines into circles, thereby realizing the targeted spatio-temporal spectra S_1, S_2, and S_3. *(B) From Yessenov et al. (2022a).*

3. Coherent space-time wave packets of nontrivial topology

In the previous section, we reviewed the physics of spatiotemporal light sheets. Here we consider more complex space-time wave packets with the fields of nontrivial topology. Many of these STWPs require temporal dispersion of the medium to act in lockstep with diffraction and thereby ensure robustness of their topological structure on propagation. The vast majority of such structured space-time STWPs can be theoretically described and their experimental implementation understood in a unified way employing the angular spectrum concept. We then start with a brief tutorial review of the angular spectrum representation of space-time paraxial wave packets in linear dispersive media.

3.1 Angular spectrum representation of paraxial wave packets in linear dispersive media

The evolution of a linearly polarized electric field E of a wave packet propagating in a linear isotropic, weakly dispersive medium is governed, in the space-frequency representation, by the Helmholtz wave equation. The latter can be written in the scalar approximation, appropriate for linearly polarized fields, as

$$\nabla'^2 E + \beta^2(\omega')E = 0. \tag{19}$$

Here $\beta(\omega')$ is a propagation constant of a plane wave of frequency ω' in the medium. Hereafter until the end of this subsection, we denote all dimensional independent variables in either physical or Fourier space with primes. Assuming paraxiality of the wave packet, propagating in the z-direction, we can express the field E in terms of its slowly-varying space-time envelope U as

$$E(\mathbf{r}', t') = U(\mathbf{r}', t')e^{i(\beta_0 z' - \omega_0' t')}, \tag{20}$$

where ω_0' is a carrier frequency, $\beta_0 = \beta(\omega_0')$, and we can write Ψ in terms of its angular spectrum $\mathcal{A}(\mathbf{k}_\perp', \Omega')$ as follows:

$$U(\mathbf{r}', t') = \int d\mathbf{k}_\perp' \int d\Omega' \, \mathcal{A}(\mathbf{k}_\perp', \Omega')e^{iq_z z'}e^{i\mathbf{k}_\perp' \cdot \mathbf{r}_\perp'}e^{-i\Omega' t'}. \tag{21}$$

Here $q_z = k_z' - \beta_0$, $\Omega' = \omega' - \omega_0'$; $\mathbf{r}' = (\mathbf{r}_\perp', z')$, $\mathbf{r}_\perp' = (x', y')$ being a position vector in a transverse plane of the wave packet and $\mathbf{k}_\perp' = (k_x', k_y')$ the corresponding wave vector.

The wave vector of each plane wave within the angular spectrum of the packet satisfies the dispersion relation

$$k_z'^2 + \mathbf{k}_\perp'^2 = \beta^2(\Omega'). \tag{22}$$

Next, in the weak dispersion and hence negligible absorption limit, we can expand the propagation constant as

$$\beta(\Omega') \simeq \beta_0 + \beta_1\Omega' + \beta_2\Omega'^2/2. \tag{23}$$

Here β_1 and β_2 describe the (inverse) group velocity at frequency ω_0' and group velocity dispersion, respectively, while the paraxiality of the envelope, together with Eq. (23), allows us to transform Eq. (22) to

$$q_z \simeq \beta_1\Omega' + \beta_2\Omega'^2/2 - \mathbf{k}_\perp'^2/2\beta_0. \tag{24}$$

On substituting from Eqs. (23) and (24) into Eq. (21), we can cast the angular spectrum representation for U into the form

$$U(\mathbf{r}', t') = \int d\mathbf{k}'_\perp \int d\Omega' \mathcal{A}(\mathbf{k}'_\perp, \Omega') e^{i(\mathbf{k}'_\perp \cdot \mathbf{r}'_\perp - \Omega'\tau')} e^{iz'(\beta_2\Omega'^2 - \mathbf{k}'^2_\perp/\beta_0)/2}, \quad (25)$$

where we introduced a retarded time by the expression $\tau' = t' - \beta_1 z'$.

Most of the STWPs generated in the laboratory to date correspond to coupling the temporal frequencies with spatial frequencies in one transverse dimension, x, say, which can be expressed in the angular spectrum as

$$\mathcal{A}(\mathbf{k}'_\perp, \Omega') = \mathcal{A}(k'_x, \Omega')\mathcal{B}(k'_y), \quad (26)$$

where $\mathcal{B}(k'_y)$ is a (spatial) angular spectrum of the field envelope in a decoupled transverse dimension. This k-space factorization, together with Eq. (25), implies factorization in physical space:

$$U(\mathbf{r}', t') = \Psi(x', t')\, Y(y'), \quad (27)$$

that is, the evolution of the decoupled field envelope is "frozen" in time. We can then treat the STWP envelope in (x', t') subspace separately. With this purpose, it is convenient to transform to dimensionless variables by scaling the coordinates (x', y', τ') and (k'_x, k'_y, Ω') in physical and k-spaces, respectively, to characteristic scales σ_x, σ_y and σ_t as: $x = x'/\sigma_x$, $y = y'/\sigma_y$ and $\tau = \tau'/\sigma_t$, as well as $K = k'_x\sigma_x$, $k_y = k'_y\sigma_y$ and $\Omega = \Omega'\sigma_t$. Further, introducing characteristic diffraction and dispersion lengths by $L_x = 2\beta_0\sigma_x^2$, $L_y = 2\beta_0\sigma_y^2$ and $L_t = 2\sigma_t^2/|\beta_2|$, we can scale the longitudinal coordinate as $z = z'/L_d$ where $L_d = \sqrt{L_x L_t}$. We can then cast the field envelope in dimensionless coordinates into the form

$$\Psi(x, \tau) = \int dK \int d\Omega\, \mathcal{A}(K, \Omega) e^{i(Kx - \Omega\tau)} e^{iz(as\Omega^2 - K^2/a)}, \quad (28a)$$

$$Y(y) = \int dk_y\, \mathcal{B}(k_y) e^{ik_y y} e^{-izbk_y^2}. \quad (28b)$$

Here $s = \mathrm{sgn}(\beta_2)$, with $s = -1$ corresponding to anomalous dispersion and $s = 1$ to normal one; $a = \sqrt{L_x/L_t}$ and $b = \sqrt{L_x L_t / L_y^2}$ are stretching factors quantifying relative strength of diffraction and dispersion. We can infer from Eqs. (28) that given the angular spectrum of the source and the type of medium dispersion, the physics of any envelope evolution is completely determined by two dimensionless stretching factors a and b. In particular, if the source field is collimated along the "frozen" spatial dimension, so that $L_y \to \infty$, a and $\mathcal{A}(K, \Omega)$ completely govern the STWP evolution in the medium.

We can show that the angular spectrum representation (28a) is equivalent to a paraxial wave equation for the field envelope that reads

$$ia\partial_z\Psi + \partial^2_{xx}\Psi - sa^2\partial^2_{\tau\tau}\Psi = 0. \tag{29}$$

Following (Lotti et al., 2010; Ponomarenko & Hebri, 2024), we can introduce the amplitude and phase Φ of Ψ to obtain a continuity equation for the energy density $|\Psi|^2$ as

$$\partial_z|\Psi|^2 + \nabla\cdot\mathbf{P} = 0, \tag{30}$$

where the energy density flux is given by the expression

$$\mathbf{P} = (2a^{-1}\mathbf{e}_x\partial_x\Phi - 2as\mathbf{e}_\tau\partial_\tau\Phi)|\Psi|^2. \tag{31}$$

Alternatively, $\mathbf{P}$ can be expressed as

$$\mathbf{P} = \mathbf{e}_x P_x + \mathbf{e}_\tau P_\tau, \tag{32}$$

where

$$P_x = -ia^{-1}(\Psi^*\partial_x\Psi - \Psi\partial_x\Psi^*), \tag{33a}$$

$$P_\tau = -isa(\Psi\partial_\tau\Psi^* - \Psi^*\partial_\tau\Psi). \tag{33b}$$

The energy density flux induced by the field of a wave packet is among its key characteristics. Specifically, the circulation of $\mathbf{P}$ around a vortex core is a fundamental signature of any spatiotemporal optical vortex.

In practice, it is rather challenging to couple an STWP into an optical fiber to take advantage of the medium dispersion. Hence, STWPs are often generated in free space by imposing a linear frequency chirp on the field in the observation plane. The STWPs with desired characteristics in a dispersive medium can then be realized in free space at an adjustable distance away from the source due to a formal analogy between Fresnel diffraction of chirped pulsed beams in free space and the propagation of the corresponding chirp free pulsed beams in linear dispersive media. To appreciate this point, let us consider a paraxial field with a space-frequency profile (in dimensional variables) $\widetilde{U}_0(x', y', \Omega')$ at the source. We can express the field profile in the transverse plane $z' = L$ by the Fresnel diffraction integral as

$$\widetilde{U}(\mathbf{r}', \Omega', L) \propto \int d\mathbf{r}''\, \widetilde{U}_0(\mathbf{r}'', \Omega')\exp\left[\frac{ik_0}{2L}(\mathbf{r}' - \mathbf{r}'')^2\right], \tag{34}$$

where we dropped an irrelevant prefactor. On the other hand, the spatiotemporal profile of the field in the plane $z' = L$ is

$$U(\mathbf{r}', \tau', L) \propto \int d\Omega' \, \widetilde{U}(\mathbf{r}', \Omega', L) e^{-i\alpha\Omega'^2} e^{-i\Omega'\tau'}. \tag{35}$$

Here we imparted a linear phase chirp α on the field in the space-frequency domain. It follows from Eqs. (34) and (35) after elementary rearrangement that

$$U(\mathbf{r}', \tau', L) \propto \int d\Omega' \int d\mathbf{r}'' \, \widetilde{U}_0(\mathbf{r}'', \Omega') e^{-i(k_0\mathbf{r}'\cdot\mathbf{r}''/L+\Omega'\tau')} e_i\left[k_0\mathbf{r}''^2/2L-\alpha\Omega'^2\right]. \tag{36}$$

We can then infer at once by comparing Eqs. (36) and (25) that provided the vector $-k_0\mathbf{r}''/L$ in physical space is identified with the transverse wave vector $k'_\perp$ and the source field in the space-frequency representation with the angular spectrum, the same STWPs can be sculpted in free space at $z' = L$ and a dispersive medium with GVD β_2. The required effective frequency chirp must obey the equation $\alpha = \beta_2 L$. We stress however, that most spatiotemporal topological light structures are not robust against free-space propagation due to uncompensated diffraction. Hence, the STWPs of tailored topology can only be generated in free space in a single transverse plane, albeit at an adjustable position.

3.2 Spatiotemporal optical vortices

Spatial optical vortices (OV) possess hollow cores and twisted helicoidal wavefronts; the electromagnetic energy of any OV circulates around its vortex core. A seminal discovery of the orbital angular momentum (OAM) of any Laguerre-Gaussain (LG) light beam (Allen et al., 1992a), which is but a prominent example of an optical vortex, has triggered exploding interest in the physics of optical vortices and their OAM content (Yao & Padgett, 2011; Padgett, 2017). The OAM of a spatial OV is usually pointed along its propagation direction; such orbital angular momenta are known as longitudinal (Bliokh & Nori, 2015).

At the same time, STWPs can be endowed with spatiotemporal OVs which carry transverse OAM. Any transverse OAM is directed along one of the two orthogonal directions in a transverse plane of a paraxial STWP. Space-time optical vortices (STOV) carrying transverse OAM were experimentally realized in pioneering experiments first in a nonlinear medium (Jhajj et al., 2016) and later in free space (Hancock et al., 2019; Chong et al., 2020). To gain insight into the STOV structure and its free-space generation, we consider the angular spectrum representation of the field of a simple STOV. Following

(Ponomarenko & Hebri, 2024), we express the dimensionless coordinates featuring in Eq. (28) in terms of the corresponding stretched polar coordinates,

$$K = a^{1/2}\kappa \cos\theta, \quad \Omega = a^{-1/2}\kappa \sin\theta; \tag{37a}$$

$$x = a^{-1/2} r \cos\phi, \quad \tau = a^{1/2} r \sin\phi, \tag{37b}$$

in the Fourier and physical spaces, respectively. It follows at once from Eqs. (37b) that

$$r = \sqrt{a x^2 + \tau^2/a}, \quad \phi = \arctan(a^{-1}\tau/x). \tag{38}$$

In the anomalous dispersion regime $s = -1$, the energy flux components, see Eqs. (33), can be cast into the form

$$P_x = -i a^{-1}(\Psi^* \partial_x \Psi - \Psi \partial_x \Psi^*), \tag{39a}$$

$$P_\tau = -i a(\Psi^* \partial_\tau \Psi - \Psi \partial_\tau \Psi^*). \tag{39b}$$

Notice the symmetry between the energy flow components up to overall scaling. Further, introducing a dimensionless "position" vector in the $x - \tau$ plane as

$$\mathbf{r} = x\mathbf{e}_x + \tau\mathbf{e}_\tau, \quad \mathbf{e}_x \times \mathbf{e}_\tau = \mathbf{e}_y, \tag{40}$$

we can define the OAM density by the expression

$$\mathbf{L} = \mathbf{r} \times \mathbf{P}. \tag{41}$$

It follows from Eqs. (38), (39) and the OAM definition upon converting to stretched polar coordinates and evaluating the appropriate derivatives that we can express the OAM density of any spatiotemporal wave packet as

$$\mathbf{L} = -i\mathbf{e}_y(\Psi^* \partial_\phi \Psi - \Psi \partial_\phi \Psi^*), \tag{42}$$

which describes an OAM transverse to the $x - \tau$ plane, T-OAM of any STOV with complex profile $\mathbf{\Psi}$.

The field of a simple STOV of topological charge l at the source,

$$\Psi(r, \phi) \propto r^{|l|} e^{-r^2/4} e^{-il\phi}, \tag{43}$$

can then be shown, with the aid of Eq. (28), to stem from the following angular spectrum:

$$\mathcal{A}(\kappa, \theta) \propto \kappa^{|l|} e^{-\kappa^2} e^{il\theta}. \tag{44}$$

Thus, the angular spectrum endowed with a twist vortex phase $e^{il\theta}$ yields an STOV. This principle can be implemented in experiment quite generally, regardless of a particular radial profile of the angular spectrum, by realizing a spatiotemporal Hankel transform of an appropriately sculpted angular spectrum (Chong et al., 2020). We sketch a spatiotemporal "Hankel transformer" setup in Fig. 10. A collimated light pulse is first spectrally resolved by a grating G and imaged onto an SLM by a cylindrical lens CL. The SLM, loaded with an appropriate hologram and working in a reflection mode, yields an STOV with transverse OAM. We note that in practice, only a time-to-frequency Fourier transform was realized with the grating and cylindrical lens. This, in conjunction with an SLM and an inverse frequency-to-time Fourier transform, produced an STOV because a spatial Fourier transform was simply implemented via free-space propagation between the source and observation plane.

The experiments of (Chong et al., 2020) demonstrate that only the fundamental vortex with $l = 1$ maintains its structure in free space. The higher-order OV loses its integrity, eventually breaking up into two fundamental ones due to unbalanced diffraction. This break-up of a higher-order STOV vortex into fundamental ones was theoretically and experimentally studied in detail in (Hancock et al., 2021; Huang et al., 2022). The lack of dispersion-induced matching temporal chirp of such an STOV brings out the formation of a stable multi-lobe structure tilted at an angle to the x-axis, each lobe corresponding to a fundamental STOV. The number of lobes and tilt angle depend on the magnitude and sign of the topological charge of the higher-order STOV. This process is reminiscent of the disintegration of higher-order spatial OVs caused by external perturbations (Nye & Berry, 1974).

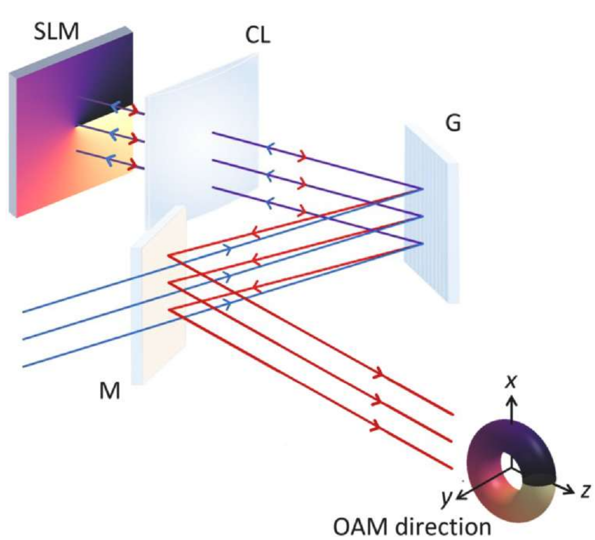

Fig. 10 Sketching an experimental setup to generate a spatiotemporal optical vortex. SLM: spatial light modulator; CL: cylindrical lens; G: grating; M: mirror.

Propagation of simple STOVs of Eq. (43) with any topological charge l in either free-space or linear dispersive media was theoretically examined (Porras, 2023; Hyde & Porras, 2023), as well as their self-focusing in nonlinear media (Le et al., 2024). Further, the evolution of Bessel STOVs was studied theoretically and experimentally in free space (Bliokh, 2021; Cao et al., 2022; Chen et al., 2022) and dispersive media (Ponomarenko & Hebri, 2024). Bessel STOVs are sculpted using the angular spectrum of plane waves confined to a unit circle in dimensionless variables in k-space, such that

$$\mathcal{A}_{\mathrm{B}}(\kappa, \theta) \propto \delta(\kappa - 1) e^{il\theta}. \tag{45}$$

Such STOVs are strictly propagation invariant in anomalously dispersive media (Ponomarenko & Hebri, 2024), maintaining their vortex profile ideally in perpetuity,

$$\Psi_{\mathrm{B}}(r, \phi, z) \propto J_l(r) e^{-il\phi}, \tag{46}$$

where $J_l(x)$ is a Bessel function of the first kind of order l. However, just as simple STOVs, Bessel STOVs of higher-order break up into elementary fundamental vortices in free space due to inherent imbalance between their non-spreading temporal and diffracting spatial dimensions. The OAM content of Bessel STOVs was also investigated, and spin-orbit interaction revealed (Bliokh, 2021).

Unfortunately, ideal Bessel STOVs carry infinite energy and hence cannot be experimentally implemented. However, Bessel-Gaussian STOVs, corresponding to the angular spectrum at the source,

$$\mathcal{A}_{\mathrm{BG}} \propto I_l(2p\kappa) e^{-p\kappa^2} e^{il\theta}, \tag{47}$$

where $I_l(x)$ is a modified Bessel function of order l and p is a real parameter, carry a finite energy and hence are realizable in the laboratory. The evolution of Bessel-Gaussian STOVs in anomalously dispersive media has been theoretically studied (Ponomarenko & Hebri, 2024). We can infer from Fig. 11 that provided $p \gg 1$, such STOVs can maintain their vortex structure in the medium over long distances. Yet, the energy flow around their cores eventually transforms from circular to radial.

Laguerre-Gaussian STOVs constitute another interesting class of space-time optical vortices that has been produced experimentally (Liu et al., 2024b). The source angular spectrum required to design such STOVs reads

$$\mathcal{A}_{\mathrm{LG}}(\kappa, \theta) \propto \kappa^{|l|} e^{-\kappa^2} L_p^{|l|}(2\kappa^2) e^{il\theta}, \tag{48}$$

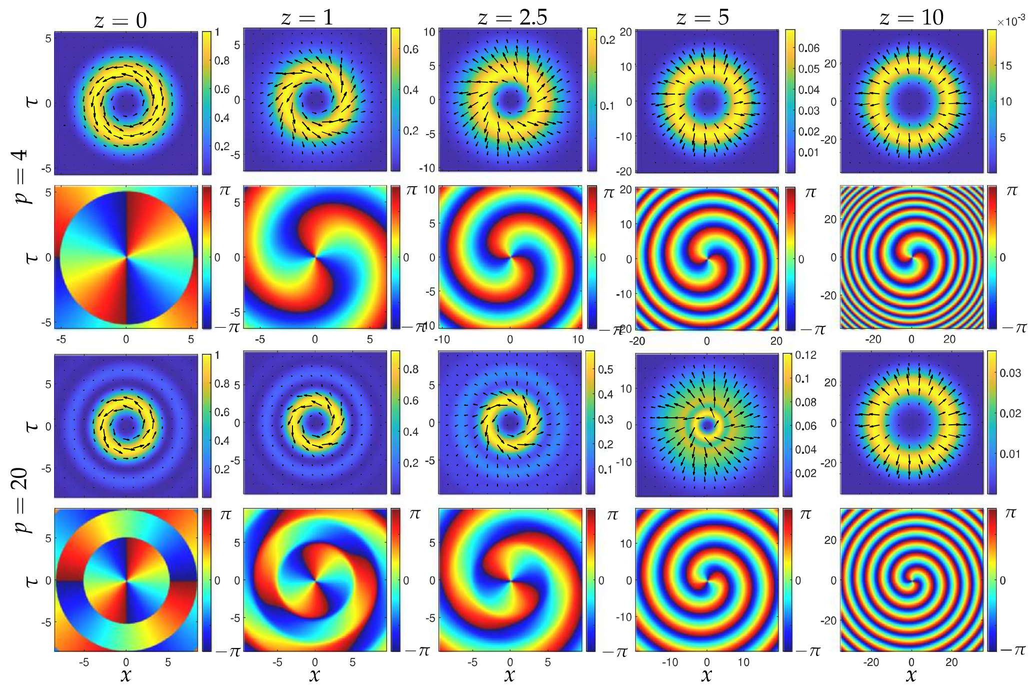

Fig. 11 Evolution of the intensity (top and second from the bottom rows), phase (second from the top and bottom rows), and energy density flow (depicted by arrows over the intensity profiles) of space-time Bessel-Gaussian vortices with $l = 2$, $a = 1$, and variable p.

where $L_p^l(x)$ is an associate Laguerre polynomial. Here l is a topological charge and p is a radial quantum number. Instructively, the field envelope of each Laguerre-Gaussian STOV is shape-invariant on propagation in a medium with anomalous dispersion. Indeed, we can express the field envelope of the Laguerre-Gaussian STOV in the following explicit form:

$$\Psi_{\mathrm{LG}}(r, \phi, z) \propto \frac{1}{w}\left(\frac{r}{w}\right)^{|l|} L_p^{|l|}\left(\frac{r^2}{2w^2}\right) e^{-r^2/4w^2} e^{ir^2/4R} e^{-il\phi} e^{i\Phi}, \tag{49}$$

where

$$w(z) = \sqrt{1 + z^2}, \tag{50}$$

and

$$R(z) = z + 1/z, \tag{51}$$

are the envelope width at the waist and its radius of curvature, respectively. Further, we define a Gouy phase by the expression

$$\Phi(z) = (2p + |l| + 1)\arctan z. \tag{52}$$

We note that Eq. (49) is a spatiotemporal analog of a conventional Laguerre-Gaussian beam frequently encountered in the laser resonator theory (Siegman, 1986) and diffractive optics (Amiri et al., 2025).

The shape invariance of these STOVs is evident from Eq. (49) by inspection and we also visualize it in Fig. 12. However, we can also infer from Fig. 12 that the electromagnetic energy flow around the core of any Laguerre-Gaussian STOV gradually transforms to a radial pattern on propagation as well. The transverse OAM of such an STOV is controlled by two quantum numbers p and l, and hence it has a more complex structure than that of a Bessel STOV. The former is comprised of two antiparallel components (Liu et al., 2024b). The spatiotemporal profiles of the STOVs that we have discussed to this point are strongly affected by their OAM content. However, the so-called perfect STOVs, whose spatiotemporal intensity distributions are virtually independent of their topological charge, have been recently theoretically explored as well (Ponomarenko & Hebri, 2024). A perfect STOV forms a narrow ring in the $(x-\tau)$ plane with neither its radius nor thickness depending on its topological charge. This theoretical work was followed by the experimental realization of perfect

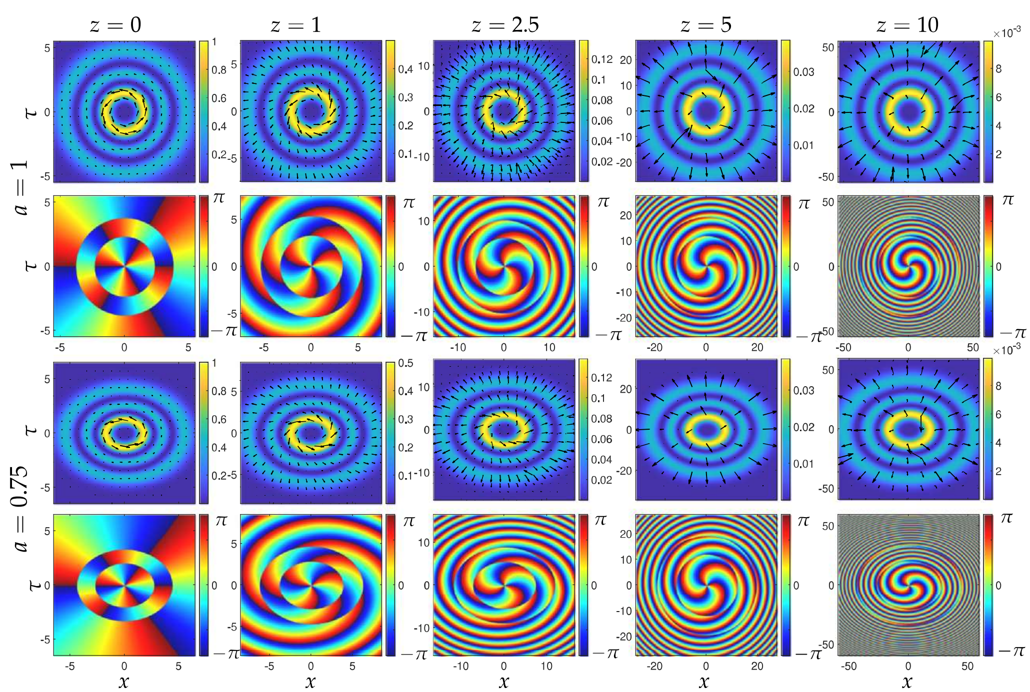

Fig. 12 Evolution of the intensity (top and second from the bottom rows), phase (second from the top and bottom rows), and energy density flow (depicted by arrows over the intensity profiles) of spatiotemporal Laguerre-Gaussian vortices with $l = 3$, $p = 2$, and variable a.

STOVs employing spertiotemporal Fourier transform of Bessel-Gaussian STOVs (Fan et al., 2025). Further, the generation of lattices of said STOVs was demonstrated by having perfect STOVs collide and reconnect.

So far, we have considered STOVs with purely transverse OAM. It turns out that STOVs with a customized OAM direction can be structured (Wan et al., 2022b) by combining two intersecting phase singularities in the $x-y$ and $x-z$ planes, respectively. The resulting STOV has two orthogonal crossing vortex lines which enables the OAM orientation control. An alternative approach is to sculpt an STOV with the OAM oriented along any desired direction of a nodal line (Wang et al., 2021). Yet another approach uses a pair of counter-rotating cylindrical lenses to establish a STOV with an arbitrary OAM tilt (Zang et al., 2022). Recently, a method has been proposed to control STOV orientation with a lens-induced spatial chirp during STWP focusing that makes it possible to rotate a longitudinal OAM over an adjustable angle (Porras & Jolly, 2023).

Reflection and refraction of conventional wave packets from an interface separating two dielectric media are known to cause small beam shifts and pulse delays, including spatial and angular Goos-Hänchen and Imbert-Fyodorov shifts, as well as Wigner time delays (Bliokh & Aiello, 2013). A temporal analogue of the Goos-Hänchen shift has also been theoretically discovered (Ponomarenko et al., 2022) and experimentally demonstrated (Qin et al., 2024) for pulses undergoing total internal reflection from a moving continuous or discrete temporal boundary. The spatial shifts are typically of the order of a wavelength and must be amplified to be measured with the aid of weak measurement techniques. The presence of a longitudinal OV in an incident wave packet boosts the magnitude of any beam shift by a factor equal to the magnitude of the topological charge of the vortex, $|l|$.

The STOVs carrying intrinsic transverse OVs experience beam shifts with unique characteristics which depend on the orientation of their OAM with respect to the plane of the interface separating the two media. Two cases should be distinguished: (a) the OAM of an STOV is orthogonal to the interface and (b) the OAM lies in the interface plane. The OAM direction of a reflected STOV is inverted in case (a) and remains the same in case (b). STOVs experience all the beam shifts and time delays familiar from studies of separable Gaussian wave packets, as well as three additional shifts that depend on the magnitudes of their topological charges (Mazanov et al., 2022). The first extra shift arises from the conservation of the z-component of the total angular momentum of an STOV. The orbital

Hall effect induces a transverse y-shift of a refracted STWP which, in turn, generates an extrinsic OAM to compensate for imbalance between z-components of the intrinsic OAM of incident and transmitted pulses. The magnitude of this shift is of the order of the carrier wavelength. The second additional shift originates from coupling between the angular Goos-Hänchen and spin-Hall (Imbert-Fyodorov) shifts and involves an amplification factor of $(1 + |l|)$; this effect scales inversely with the Rayleigh range of the STWP. Finally, there are longitudinal shifts of STOVs refracted/reflected from the interface, which are spatial analogues of Wigner time delays. While the latter requires medium dispersion, the former originate from spatial dispersion and hence are of a purely geometric nature.

3.3 Toroidal vortices of light

Vortex rings have attracted widespread attention of the scientific community since Lord Kelvin's original classical vortex model of an atom (Kelvin, 1867). Vortex rings arise in the context of modeling as diverse and complex objects and phenomena as human heart (Kilner et al., 2000), underwater air bubbles (Lim & Nickels, 1992) and volcanic eruptions (Taddeucci et al., 2021). Such rings feature prominently in the physics of quantum superfluids as well (Nemirovskii, 2013). Optical vortex rings have also been studied in connection with dipole and multipole optical excitations in metamaterials (Miroshnichenko et al., 2015; Huang et al., 2013; Watson et al., 2016).

Propagating vortex rings, also termed toroidal vortices of light, have been reported recently (Wan et al., 2022a). The experimental protocol of (Wan et al., 2022a) involves a conformal mapping of straight cylindrical vortex tubes to torii employing the Cartesian-to-log polar conformal transformation identical to that used to generate axially symmetric STWPs localized in all dimensions (Yessenov et al., 2022a). The resulting envelope of any toroidal light vortex, expressed in dimensionless variables, reads

$$\begin{aligned}\Psi(r,\tau) \;\propto\; & [(r-r_0)^2+\tau^2]^{|l|/2}\exp\left[-\frac{(r-r_0)^2+\tau^2}{2z_0}\right] \\ \times\; & \exp\left[-il\arctan\left(\frac{\tau}{r-r_0}\right)\right],\end{aligned} \tag{53}$$

where r is a radial (transverse) coordinate, r_0 is a vortex core radius, τ is time, z_0 is a characteristic (dimensionless) transverse scale, and l is a topological charge of the vortex. In Figs. 13 and 14, we exhibit the simulated and measured intensity profiles of such a vortex ring. The vortex

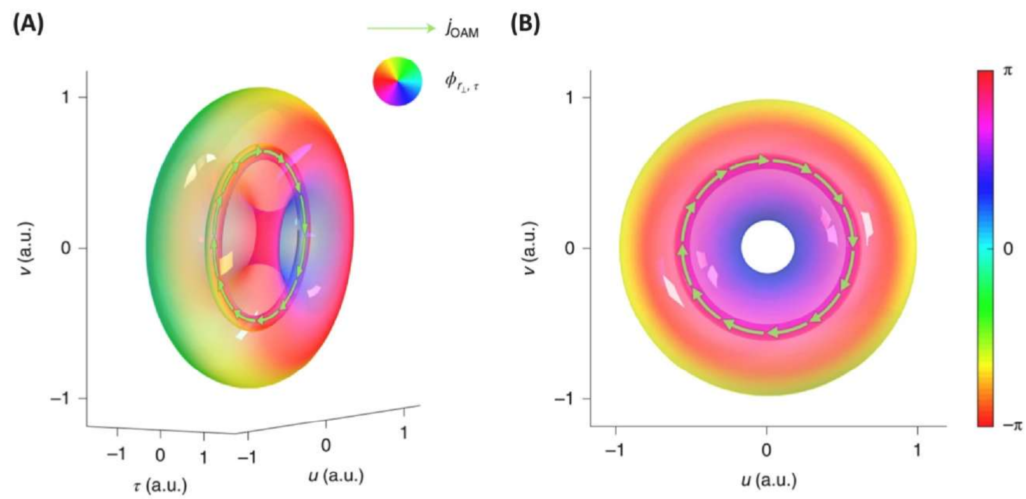

Fig. 13 (A) Side view of the 3D iso-intensity profile of a photonic toroidal vortex. The colors denote the rotating spatiotemporal spiral phase ϕ. The topological charge of the spiral phase is 1. The direction of local OAM density (j_{OAM}) is marked with arrows. (B) Front view of the iso-intensity profile of a photonic toroidal vortex. *(B) From Wan et al. (2022a)*

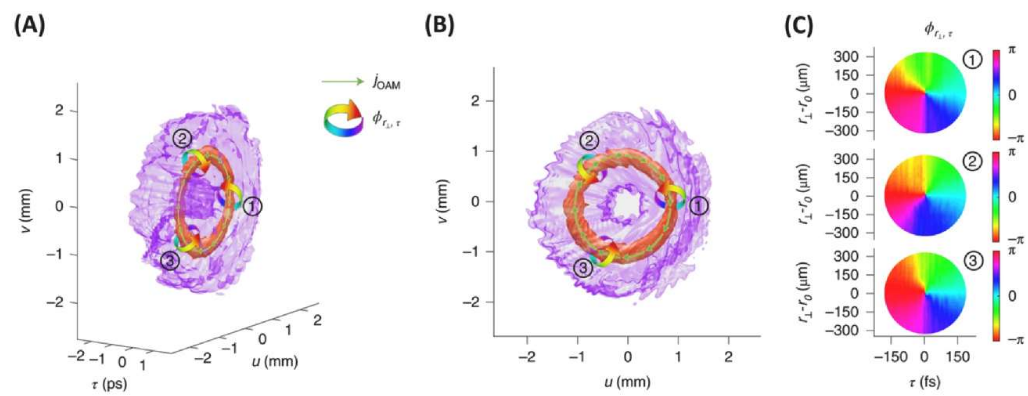

Fig. 14 (A,B), Three-dimensional iso-intensity profile of the photonic toroidal vortex from different perspectives. The maximum intensity is set to unity and the iso-value is 0.02, implying that the iso-surface profile includes all points with the intensity larger than 0.02. The spatiotemporal spiral phase Φ is marked with curved colored arrows and the local OAM density (j_{OAM}) is marked with light green arrows. (C) Circulating spiral phase in the radial-temporal plane. The topological charge of the spiral phase is 1. *(C) From Wan et al. (2022a).*

ring possesses a 3D phase structure that rotates around a closed loop, forming a ring-shaped vortex line. The toroidal STWP advances in the direction perpendicular to the ring orifice at the speed of light. The direction of local orbital angular momentum (OAM) density is marked with arrows in both figures.

3.4 Space-time toroidal and supertoroidal light wave packets

In addition to paraxial STWPs, which can be treated within a scalar slowly varying envelope approximation, there exist ultra-wideband STWPs that are exact solutions to Maxwell's equations in free space. The fields of such STWPs can be conveniently determined using Hertz potentials (Essex, 1977; Jackson, 2021).

Hereafter, we return to dimensional variables. Consider, for instance, a transverse electric (TE) polarized field of an STWP propagating in the positive z-direction. The Hertz potential $\mathbf{\Pi}_m$ must then be longitudinal, such that

$$\mathbf{\Pi}_m = \mathbf{e}_z F(\mathbf{r},\ t), \tag{54}$$

where $F(\mathbf{r},\ t)$ is a scalar potential to be determined. The TE-polarized electromagnetic fields in free space are given in terms of the Hertz potential as

$$\mathbf{E} = -Z_0 \nabla \times \partial_t \mathbf{\Pi}_m; \qquad \mathbf{H} = \nabla \times (\nabla \times \mathbf{\Pi}_m), \tag{55}$$

where $Z_0 = \sqrt{\mu_0/\epsilon_0}$ is a free-space impedance. It follows at once on substituting from Eqs. (54) and (55) into the Maxwell equations that the scalar potential $F(\mathbf{r},\ t)$ obeys a wave equation in free space,

$$\nabla^2 F - c^{-2}\partial_{tt}^2 F = 0. \tag{56}$$

Thus, the electromagnetic fields of any TE-polarized STWP can be found by solving a scalar wave equation for F. The fields of TM-polarized STWPs can be inferred from those of TE-polarized ones by the reciprocity relations: $\mathbf{E}_{\mathrm{TE}} \to -Z_0^2 \mathbf{H}_{\mathrm{TM}}$ and $\mathbf{H}_{\mathrm{TE}} \to \mathbf{E}_{\mathrm{TM}}$ (Jackson, 2021).

Ziolkowski (Ziolkowski, 1989) and Bélanger (Belanger, 1984) showed independently that by employing an Ansatz,

$$F(\mathbf{r},\ t) = e^{ik(z+ct)} F_k(\mathbf{r}_\perp,\ z - ct), \tag{57}$$

Eq. (56) can be reduced to a Schrödinger-type evolution equation in the transverse spatial coordinates $\mathbf{r}_\perp$ and retarded longitudinal coordinate $\zeta = z - ct$ as

$$(4ik\partial_\zeta + \nabla_\perp^2) F_k = 0. \tag{58}$$

Here $F_k(\mathbf{r}_\perp,\ \zeta)$ is a "mode" of Eq. (58) corresponding to a given constant k. Structured STWPs can then be expressed as linear superpositions of the modes as

$$F(\mathbf{r},\ t) = \int dk\ a(k) F_k(\mathbf{r}_\perp,\ \zeta), \tag{59}$$

where $a(k)$ is a spectrum of any mode. This modal representation is an analogue of the angular spectrum of plane waves that we have actively employed to describe slowly-varying envelope STWPs.

Ziolkowski (Ziolkowski, 1989) proposed to employ a particular set of modes, the so-called moving complex-center Gaussian sources expressed as

$$F_k(\mathbf{r}_\perp, \zeta) = \frac{e^{-kr_\perp^2/(z_0+i\zeta)}}{4\pi i(z_0 + i\zeta)}, \tag{60}$$

and a particular mode power spectrum to obtain a family of exact finite-energy STWPs generated from the scalar potential

$$F(\mathbf{r}, t) = F_0 \frac{e^{-s/q_3}}{(q_1 + i\zeta)(s + q_2)^\alpha}. \tag{61}$$

Here $s = r_\perp^2/(q_1 + i\zeta) - i(z + ct)$, and F_0, q_1, q_2 and q_3, as well as α are real constant parameters. Assigning different values to these constants yields a variety of topologically nontrivial axially symmetric STWPs.

The physical meaning of q_1 through q_3 is illustrated in Fig. 15. We can infer that q_1 specifies a temporal duration of the pulse, while q_2 gives a typical spreading (Rayleigh) range of the fields. For ultrashort, one-cycle pulses, $q_1 \ll q_2$. Further, q_3 governs the rate of transverse angular divergence of the STWP.

Historically, the first such STWPs of toroidal topology, which correspond to $q_1 \ll q_2$, $q_3 \to \infty$ and $\alpha = 1$, were found by Hellwarth and Nouchi (Hellwarth & Nouchi, 1996) who revisited Ziolkowski's solution. These toroidal pulses are known as "flying doughnuts". Their higher-order generalizations, corresponding to a set of parameters: $q_1 \ll q_2$, $q_3 \to \infty$ and $\alpha \geq 1$, were recently theoretically studied (Shen et al., 2021a) and the name supertoroidal pulses was coined.

The electric fields of toroidal and supertoroidal STWPs carry phase singularities. While the electric fields of flying doughnuts possess a bispherical singular surface, those of supertoroidal ones feature nested matryoshka-like singularities displayed in Fig. 16. In addition, the magnetic fields of supertoroidal STWPs exhibit a number of remarkable features. First of all, they manifest a hedgehog skyrmionic structure, as is evidenced by Fig. 17; various textures of N é el-type skyrmionic structures can be discerned in the figure. By the same token, the energy flow of supertoroidal pulses, governed by the corresponding Poynting vectors, displays coexisting regions of vortex-like and saddle-like flow patterns, as well as regions of backflow.

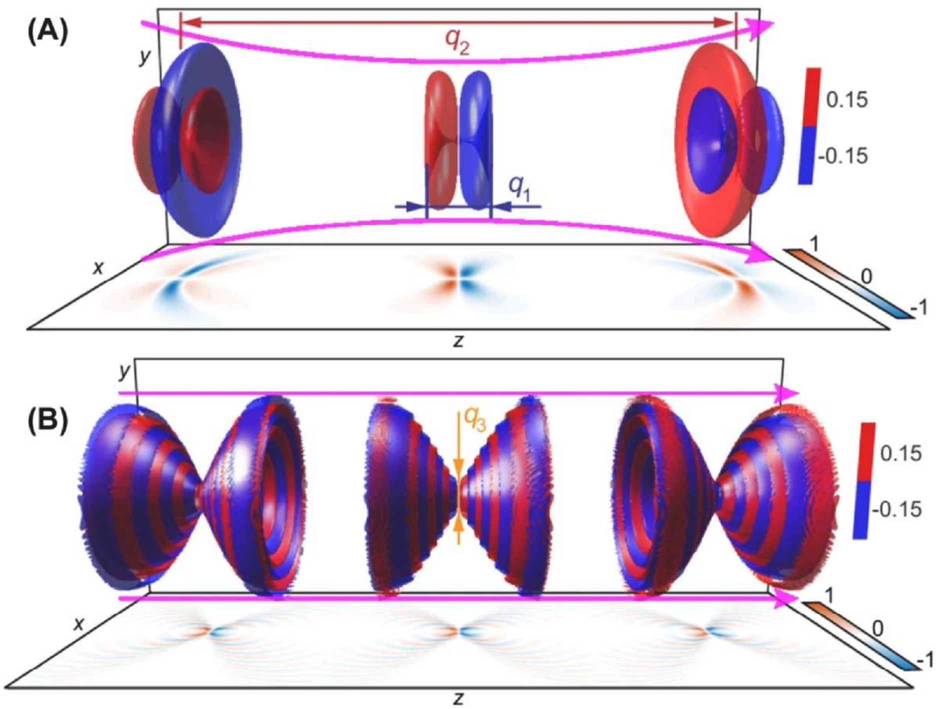

Fig. 15 Evolution of a toroidal (A) and non-diffracting supertoroidal (B) pulses: The distributions of the TE polarized electric fields of the pulses in the $x-z$ plane at $t=0, \pm q_2/2c$ are plotted. The red and blue 3D iso-surfaces represent the spatial points where the electric field amplitude, normalized to the corresponding maximum value, equals to 0.15 and −0.15, respectively. The dark blue, magenta, and yellow arrows mark the optical cycle length q_1, Rayleigh range q_2, and transverse divergence q_3, respectively. Parameters used in the simulation: A $q_2/q_1=40$; B $q_2/q_1=100$ and $q_2/q_1=1$. *(B) From* Shen et al. (2024a).

Further, the electromagnetic fields of such supertoroidal pulses exhibit fractal-like features whereby fine-scale regions of the field contain scaled-down replicas of the patterns evident on coarser scales. For example, the matryoshka pattern of the magnetic field of a superoroidal STWP is shown to be replicated on ever finer scales in Fig. 18.

As is evident from Fig. 15, higher-order STWPs with finite q_3 morph their shape from simple doughnut-like tori to X-shaped layers of tori with a narrow neck and wide wings. Counterintuitively, as q_3 decreases, so does the wavepacket divergence in the transverse plane. Eventually, as q_3 approaches the optical cycle length q_1, STWPs become virtually diffraction free (Shen et al., 2024a). Thus, the striking features of supertoroidal pulses that we have discussed can persist over long propagation distances. The correlation between finite values of q_3 and resistance to diffraction can be understood in terms of the STWP profile morphing into an X-wave: As q_3

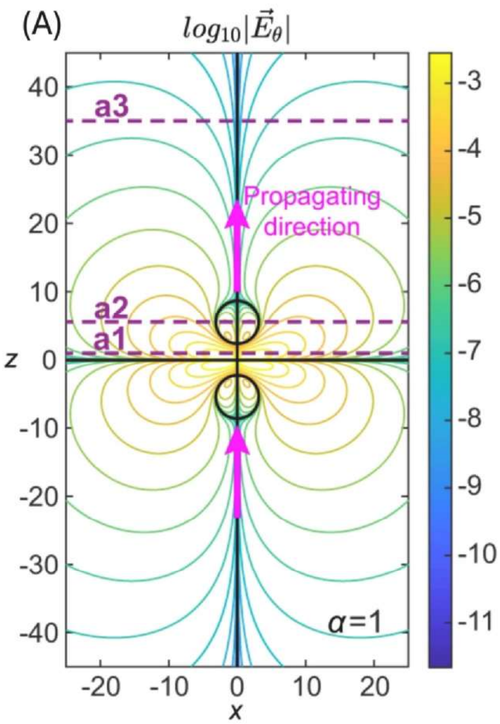

Fig. 16 (A,B) $x-z$za (A) fundamental toroidal pulse, $\mathrm{Re}[E_\theta(\mathbf{r}, t=0)]$, and (B) super-toroidal pulse with $\alpha=5$, $\mathrm{Re}[E_\theta^{(\alpha=5)}(\mathbf{r}, t=0)]$ in a logarithmic scale. The bold black lines represent zero-value singular lines. *(B) From* Shen et al. (2021a).

is reduced, so does the minimal transverse size of the structure, pushing most of the electromagnetic energy carried by the STWP toward the X-wave tails.

The magnetic fields of these non-diffracting toroidal STWPs manifest vortex-saddle energy flow and backflow patterns, as well as skyrmionic structures, see Fig. 19. Perhaps, their most striking signature, though, is the emergence of a hierarchy of vortices in their magnetic field distributions. This moving vortex hierarchy resembles a celebrated Kármán vortex street which is ubiquitous in fluid mechanics (Von Kármán, 2004). In Fig. 19, we display a Poynting vector distribution, which manifests backflow regions, and the magnetic field distribution showcasing rows of vortex-like and saddle-like singularities, the former realizing an optical Kármán vortex street.

3.5 Spatiotemporal optical knots, links and hopfions

Lord Kelvin's classic model of an atom in terms of knotted electromagnetic field configurations has triggered interest in knots and links in a number of branches of classical and quantum physics from fluid mechanics (Moffatt, 1969) and plasma (Berger, 1999) to polymer (Kamien, 2002) and atomic

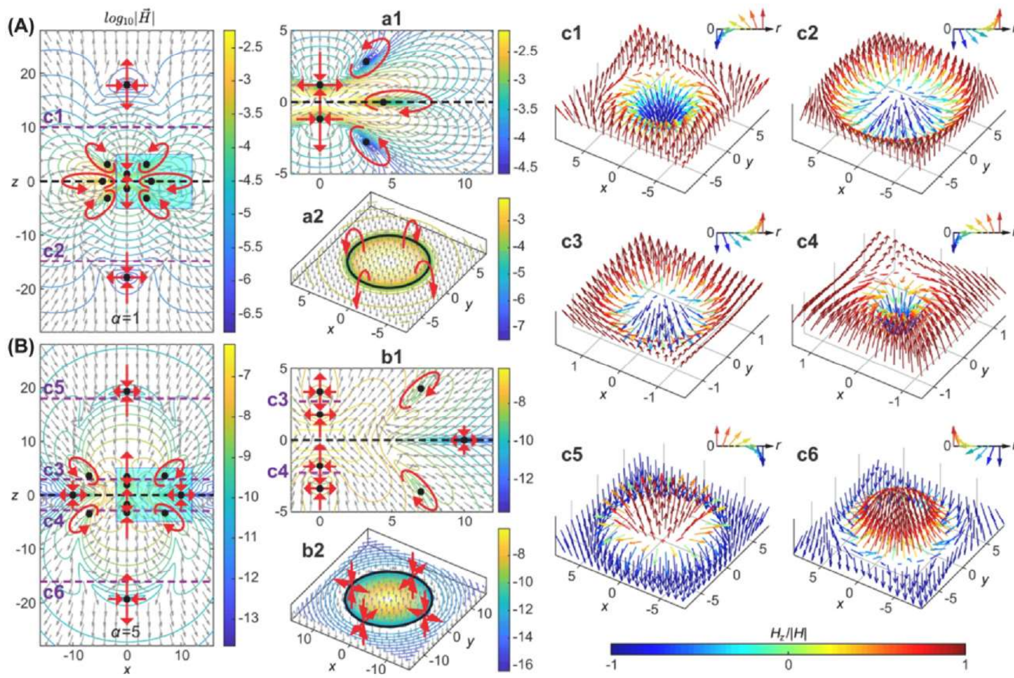

Fig. 17 Magnetic fields of toroidal (A) and supertoroidal (B) light pulses in a logarithmic scale. Phase singularites are marked by black dots with red arrows corresponding to saddle or vortex singularities; (a1) and (b1): zoom-in plots of blue boxed regions of (a and b). Panels (a2) and (b2): magnetic field amplitude distributions and normalized field directions in $z=0$ plane. (C) Various Néel-type skyrmionic textures observed in different transverse planes (see dashed purple lines in A and B) for the fundamental toroidal (c1-c2) and supertoroidal (c3–c6) pulses, shown with arrows. The upright insert of each panel shows a basic texture of the skyrmionic structure. All coordinate b hs are scaled to q_1; $a=5$. *(B) From Shen et al. (2021a).*

physics (Berry, 2001). As a result, a general theory of classical knotted fields has been formulated (Faddeev & Niemi, 1997) and further refined (Battye & Sutcliffe, 1998; Babaev et al., 2002). Linked and knotted electromagnetic fields have also been explored in connection with knotted vortex lines of the Riemann-Silberstein vector (Bialynicki-Birula & Bialynicka-Birula, 2003) and the lines of darkness in monochromatic optical fields (Berry & Dennis, 2001). The latter were experimentally realized later (Leach et al., 2004). Further, isolated knots of paraxial light beams were theoretically constructed and experimentally verified (Dennis et al., 2010).

In a series of papers (Ranada, 1989,1990), Rañada showed how an intriguing STWP can be sculpted such that the electric and magnetic field lines form closed loops with any pairs of electric—or magnetic—field lines linked. The name hopfion was coined to refer to this solution because Rañada's approach relies on the Hopf fibration. To this end, Rañada

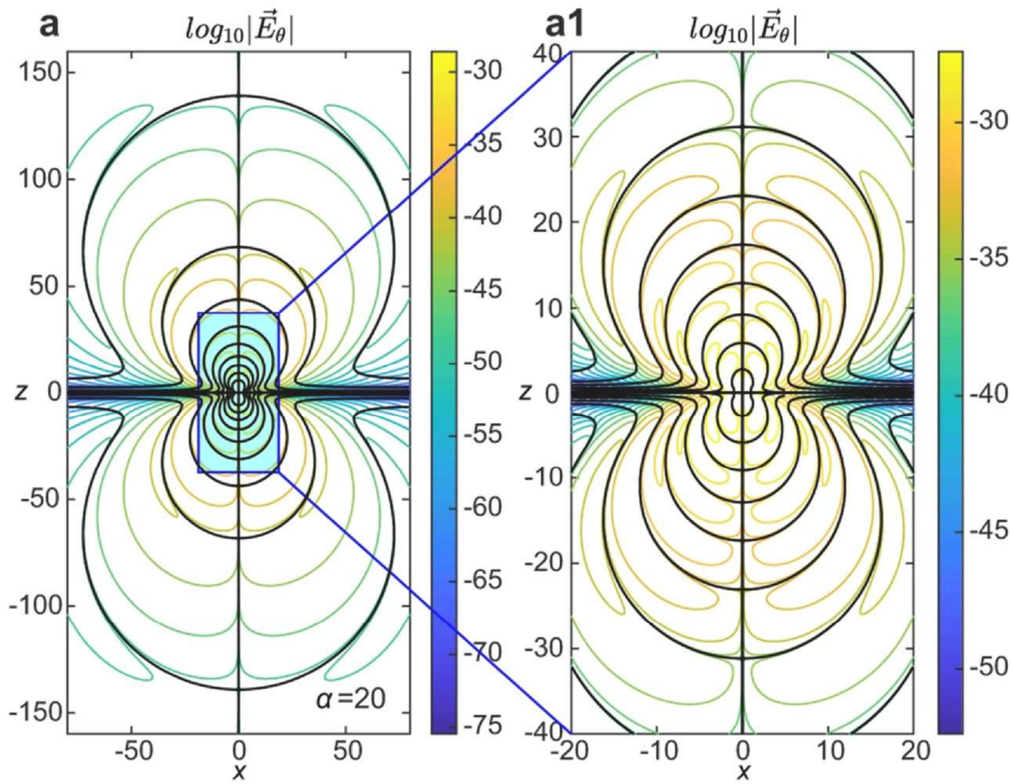

Fig. 18 Fractal-like patterns in electromagnetic fields of supertoroidal pulses. The isoline plot of the electric field in the x-z plane for the supertoroidal pulse corresponding to $\alpha = 20$, $\mathrm{Re}[E_\theta^{(\alpha=20)}(\mathbf{r},\ t = 0)]$, in a logarithmic scale. Electric field zeros are marked by the black solid lines and black dots. Panel (a1) presents a zoom-in plot of the region highlighted by the blue box in (A). *From* Shen et al. (2021a).

considered an ordinary sphere S^2 in the physical 3D space R^3, and a hypersphere S^3 in a 4D space. He then introduced a Hopf map (Urbantke, 2003), $S^3 \rightarrow S^2$ with the complex function

$$\Phi_{\mathrm{H}}(x,\ y,\ z) = \frac{2(x + iy)}{2z + i(x^2 + y^2 + z^2 - 1)}, \tag{62}$$

via a stereographic projection to construct exact solutions to the Maxwell equations in free space. It turns out that the lines of constant amplitude and phase of the map are circles and surfaces of constant amplitude are nested tori. Importantly, any two level curves of Φ_{H} are linked, resulting in a link between any two pairs of electric (magnetic) lines of a propagating wave packet.

We present the evolution of the electromagnetic field and the energy density of a thereby generated STWP in Fig. 20. At time $t = 0$, the Hopf fibration is composed of n fibers aligned with the axes x (electric field) and

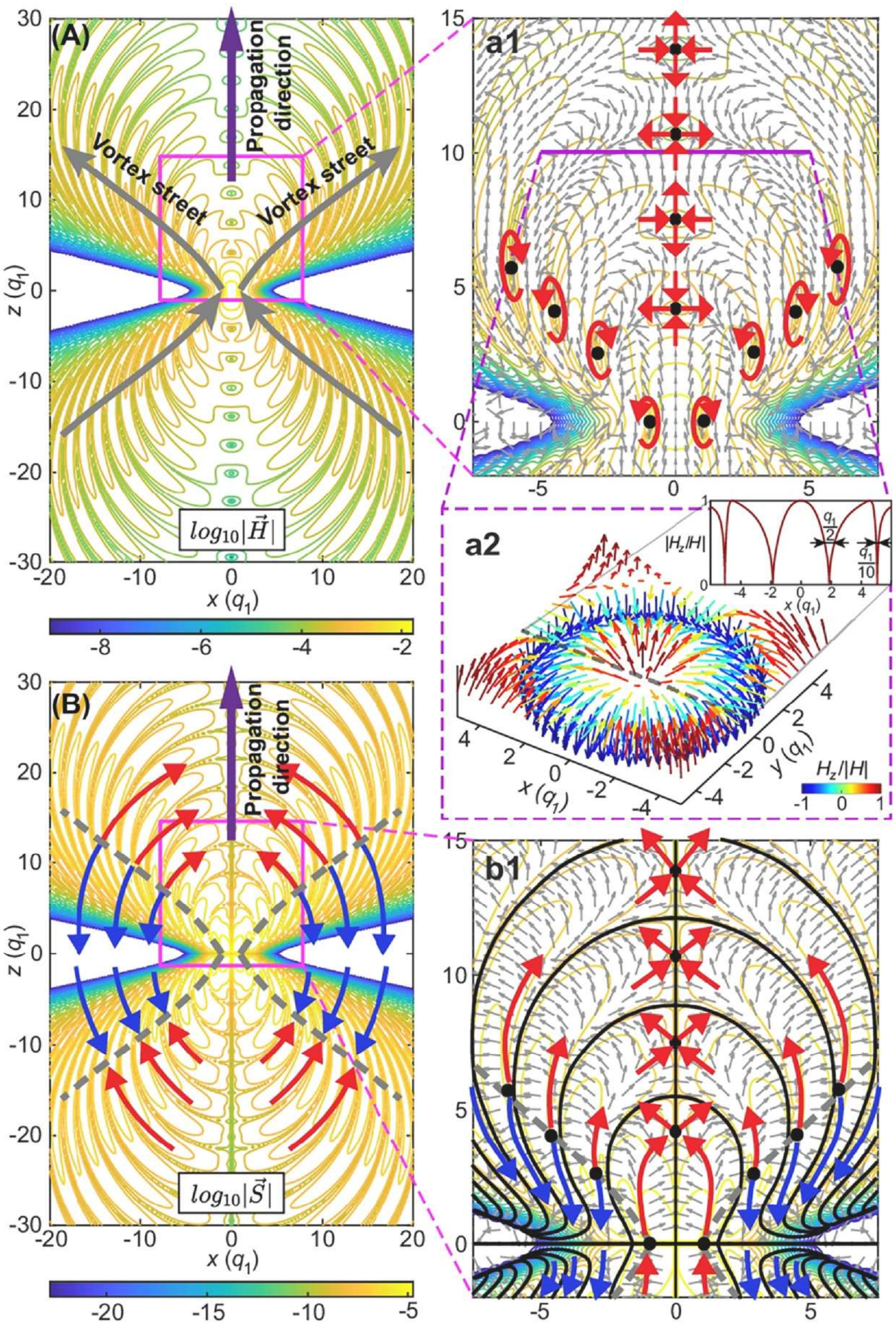

Fig. 19 Topological electromagnetic and energy flow structures. Magnetic field (A) and Poynting vector (B) distributions of a non-diffracting supertoroidal pulse with $q_2 = 100$ and $q_3 = 1$ at $t = 0$. The contours show the logarithm of the moduli of the corresponding vectors. (a1) A zoom-in of the magnetic field with arrows showing the field distribution, the black dots and red arrows marking singularities (vortex and saddle). (a2) Arrows shows a skyrmionic structure of the magnetic field in the transverse (x–y) plane at $z = 10$. (b1) A zoom-in of the Poynting vector distribution; solid lines and dots mark zeros of the Poynting vector, while red and blue arrows indicate areas with forward and backward energy flow, respectively. Unit of length: q_1. *(B) From* Shen et al. (2024a).

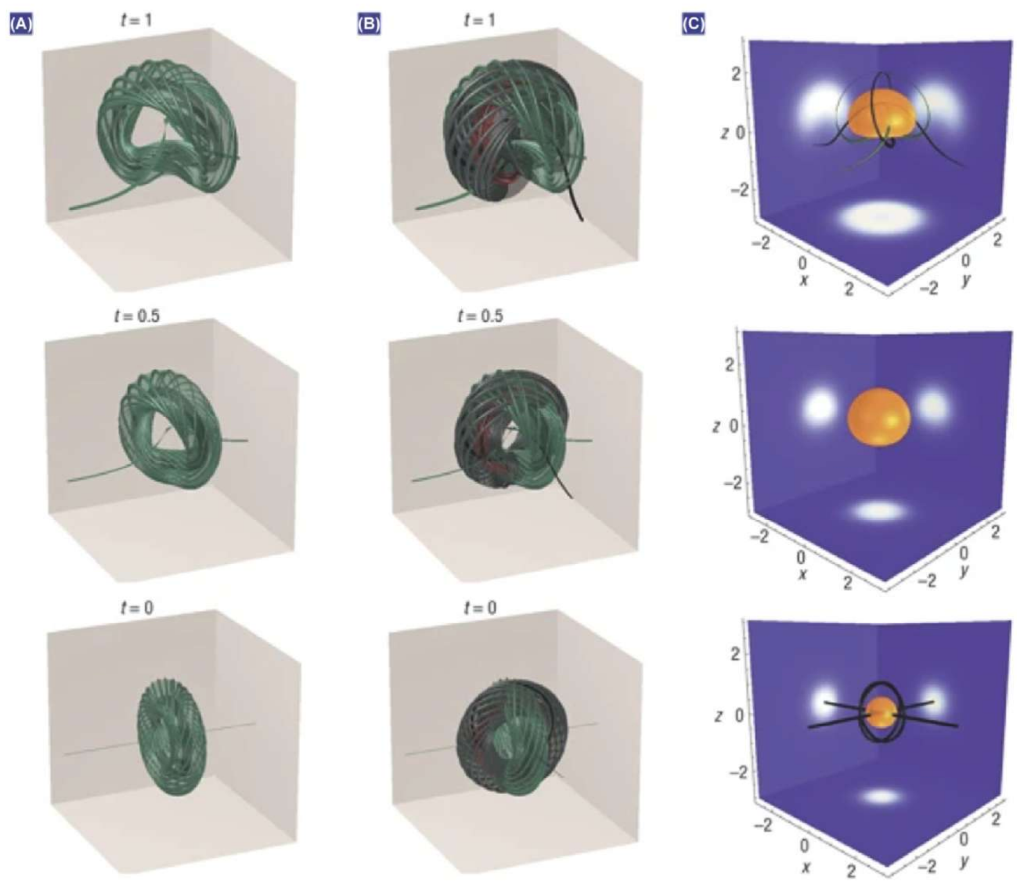

Fig. 20 Time evolution of the field lines and energy density of the Hopf knot. (A,B) Time evolution of the electric field lines (green) (A) and of the magnetic field lines (black) (B), shown together with the electric field lines for reference. (C) Time evolution of the energy density. *(C) From Irvine and Bouwmeester (2008).*

y (magnetic field), and the s fibers lying in the planes $y-z$ (electric field) and $x-z$ (magnetic field), centered at the origin. The linked lines of the electric and magnetic fields fill two orthogonal tori that form a hopfion at any time (see Fig. 20B). In free space propagation, the density of electromagnetic energy evolves from a spherical shape to an umbrella shape, opening in the preferred propagation direction along the z-axis while preserving the Hopf structure. The energy density structure remains centered at the center of the knot as is clearly seen in Fig. 20C. The electric and magnetic field lines remain mutually orthogonal everywhere throughout the time evolution.

To gain insight into the electromagnetic field structure of a hopfion, Irvine and Bouwmeester (Irvine & Bouwmeester, 2008) derived a representation of the hopfion vector potential in terms of vector spherical harmonics (VSH). We can express the VSH modes with either electric (TE) or magnetic (TM) fields transverse to the radial direction as (Jackson, 2021)

$$A_{lm}^{\mathrm{TE}}(k, \mathbf{r}) = -\frac{i}{kc} f_l(kr) \mathbf{L} Y_{lm}(\theta, \phi), \tag{63}$$

and

$$A_{lm}^{\mathrm{TM}}(k, \mathbf{r}) = \frac{1}{k^2} \nabla \times [f_l(kr) \mathbf{L} Y_{lm}(\theta, \phi)], \tag{64}$$

where $\mathbf{L} = -ir \times \nabla$ is an OAM operator and Y_{lm} are spherical harmonics. Further, $f_l(kr)$ is a radial mode function. In free space, the latter is given by a spherical Bessel function, $f_l(kr) \propto j_l(kr)$, up to an irrelevant normalization constant. We can then decompose the vector potential of any electromagnetic field in free space into VSHs as

$$A(\mathbf{r}, t) = \int d\mathbf{k} \sum_{l,m} [a_{lm}^{\mathrm{TE}}(k) A_{lm}^{\mathrm{TE}}(k, \mathbf{r}) + a_{lm}^{\mathrm{TM}}(k) A_{lm}^{\mathrm{TM}}(k, \mathbf{r})] e^{-ikct} + c.\ c. \tag{65}$$

The authors of (Irvine & Bouwmeester, 2008) have shown that hopfions have a strikingly simple VSH decomposition in the form

$$A_{\mathrm{Hopf}}(\mathbf{r}, t) \propto \int dk k^2 a(k) [A_{1,1}^{\mathrm{TE}}(k, \mathbf{r}) - i A_{1,1}^{\mathrm{TM}}(k, \mathbf{r})] e^{-ikct} + c.\ c, \tag{66}$$

with an exceptionally simple amplitude of the energy spectrum as

$$a(k) \propto k e^{-k/k_0}, \tag{67}$$

where k_0 is a characteristic scale in the k-space.

Remarkably, the linear superposition of VHSs $A_{1,1}^{\mathrm{TE}} - iA_{1,1}^{\mathrm{TM}}$ is an eigenstate of the curl operator, such that

$$\nabla \times [A_{1,1}^{\mathrm{TE}} - iA_{1,1}^{\mathrm{TM}}] = \mp k [A_{1,1}^{\mathrm{TE}} - iA_{1,1}^{\mathrm{TM}}], \tag{68}$$

corresponding to the eigenvalue k. These eigenstates, known as Chandrasekhar-Kendall states, have played an important role in astrophysics (Chandrasekhar & Kendall, 1957), plasma physics (Moses, 1971) and fluid mechanics (Woltjer, 1958).

To grasp the physics behind the vector spherical harmonic decomposition of Eq. (66), we notice that the Chandrasekhar-Kendal states corresponding to the same k yield the electric and magnetic fields proportional, up to a 90-degree rotation, to the same vector potential, $\mathbf{B} = \nabla \times \mathbf{A} = \pm k\mathbf{A}$ and $\mathbf{E} = -\partial_t \mathbf{A} = -ikc\mathbf{A}$. It can be inferred that $A_{1,1}^{\mathrm{TE}}$ and $A_{1,1}^{\mathrm{TM}}$ follow the smaller and larger circumference of each torus. Therefore, their linear superpositions are confined to said torus as well; all superpositions corresponding to different k's will wrap around tori. The simple nodeless spectrum (67) ensures that all radial mode zeroes are suppressed and the resulting hopfion is composed of smooth loops with no oscillations or twists. Instructively, the Chanrdasekhar-Kendal states conserve helicity h_m (h_e) of the magnetic (electric) field, defined as

$$h_m \propto \int d\mathbf{r}\, \mathbf{A}\cdot\mathbf{B}; \tag{69a}$$

$$h_e \propto \int d\mathbf{r}\, \mathbf{C}\cdot\mathbf{E}, \tag{69b}$$

where the electric vector potential $\mathbf{C}$ is defined through $\mathbf{E} = \nabla \times \mathbf{C}$. The helicities quantify the degree of self-linking of the electromagnetic field. Thus, the hopfion preserves its linkage on time evolution in free space.

Higher-order STWPs can also be constructed by adding more VSH modes, beyond just Chandrasekhar-Kendall states, as well as structuring the mode power spectrum. Higher-order modes manifest knotting of individual field lines and the formation of links of the knotted lines, yielding progressively more and more complex structures. The authors of (Irvine & Bouwmeester, 2008) consider an example of a multipole field corresponding to $l = 2$ and $m = 2$, which we display in Fig. 21. An impressive complexity of the electromagnetic field structure is evidenced by Fig. 21(A-D). We also observe knotting of the field lines in Fig. 21E. Finally, the example exhibits the emergence of a doubly linked trefoil knot in the knotted tangle topology of such a composite STWP (Fig. 21F).

4. Partially coherent spatiotemporal wave packets

4.1 Space-time statistical wave packets of light

There has been growing recognition that light fields with structured spatial or temporal coherence properties can be instrumental in free-space optical communications and imaging (Shen et al., 2021b; Li et al., 2024b), information encryption, storage and transfer (Peng et al., 2021; Yao et al., 2024), and optical multiplexing (Liu et al., 2025). In particular, partially coherent beams have been shown to be extremely robust against atmospheric turbulence (Xu et al., 2022). They also manifest unparalleled self-healing capabilities (Wang et al., 2016a; Xu et al., 2020). Several classes of spatiotemporal wave packets of partially coherent light have also been theoretically introduced (Hyde, 2020) and their propagation in linear

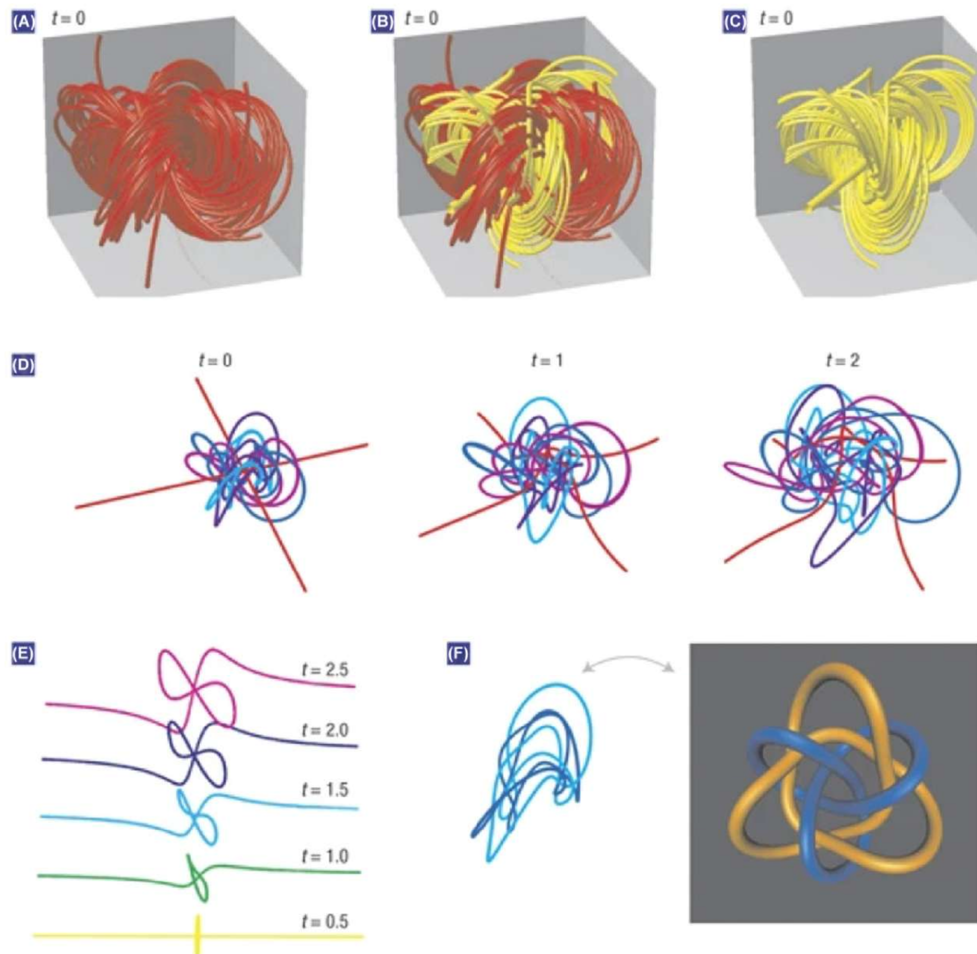

Fig. 21 Generalization of the Hopf fields on the basis of the VSPHs, obtained using $l = 2$, $m = 2$ multipole fields. (A-C, D) The magnetic (red) and electric (yellow) field lines at time t = 0. (E) The time evolution of the *s* and *n* fibers for the Hopf field for comparison. (F) Doubly linked trefoil knot generation. *(F) From Irvine and Bouwmeester (2008).*

dispersive media and atmospheric turbulence explored (Hyde et al., 2023; Hyde, 2024). Moreover, STWPs with their degree of coherence endowed with OVs have been proposed and theoretically investigated (Ding et al., 2022). It was shown that spatiotemporal coherence parameters can be adjusted to control the positions and phase distributions of such spatio-temporal coherence vortices (Ding et al., 2023).

Partially coherent, propagation-invariant space-time light sheets were theoretically explored and experimentally realized in (Yessenov et al., 2019a) employing the techniques discussed in Section 2.2. To gain insight into the structure of field correlations of such space-time sheets of statistical light, we consider the angular spectrum representation of the field envelope of any paraxial light sheet in the form

$$\Psi(x, t, z) = \int d\Omega \int dk_x \widetilde{\Psi}(k_x, \Omega) e^{ik_x x} e^{iq_z z} e^{-i\Omega t}, \tag{70}$$

where we use the notations introduced in Section 2.1. The second-order statistical properties of any ensemble of (statistically) stationary fields of space-time light sheets at pairs of space-time points (x, t) and $(x', t + \tau)$ can be described in terms of the mutual intensity, which is defined as

$$\Gamma(x, x'; \tau, z) = \langle \Psi^*(x', t + \tau, z) \Psi(x, t, z) \rangle, \tag{71}$$

where the angle brackets denote ensemble averaging. To ensure statistical stationarity, the (spatiotemporal) spectral amplitudes must be delta-correlated in the temporal frequency, such that

$$\langle \widetilde{\Psi}^*(k_x', \Omega') \widetilde{\Psi}(k_x, \Omega) \rangle = \mathcal{A}(k_x, k_x', \Omega) \delta(\Omega - \Omega'). \tag{72}$$

Further, the STWPs are propagation-invariant provided the following angular spectrum coupling is imposed (recall Section 2.2):

$$q_z = \Omega / \tilde{v}, \tag{73}$$

between any pairs of spatial and temporal frequencies within the STWP spectrum. It then follows at once from Eqs. (70) through (73) that

$$\Gamma(x, x'; \tau, z) = \int dk_x \int dk_x' \, \mathcal{A}(k_x, k_x', \Omega) e^{i(k_x x - k_x' x')} e^{-i\Omega(k_x)\tau}. \tag{74}$$

Next, recalling the dispersion relation for paraxial propagation-invariant light-sheets,

$$\Omega = \frac{k_x^2}{2k_0(c^{-1} - \tilde{v}^{-1})}, \tag{75}$$

we can infer that tight correlations between any pairs of temporal frequencies, $\Omega = \Omega'$, imply the same between the corresponding spatial frequencies, $k_x^2 = k_x'^2$. It follows that only perfectly correlated, $k_x = k_x'$, or anti-correlated, $k_x = -k_x'$ plane waves can enter the autocorrelation function $\mathcal{A}(k_x, k')$ of the angular spectrum. In other words, the angular spectrum correlations must have the structure,

$$\mathcal{A}(k_x, k_x') = \mathcal{A}_{\mathrm{bc}}(k_x) \delta(k_x - k_x') + \mathcal{A}_{\mathrm{bp}}(k_x) \delta(k_x + k_x'). \tag{76}$$

The first term on the right-hand side of Eq. (76) describes statistically stationary background noise with the (spatial) spectrum $\mathcal{A}_{\mathrm{bc}}$, while the second corresponds to a spectral bump $\mathcal{A}_{\mathrm{bp}}$ atop the background. In the space-time domain, such an angular spectrum translates to

$$\Gamma(x, x'; \tau, z) = \Gamma_{\mathrm{bc}}(x - x', \tau) + \Gamma_{\mathrm{bp}}(x + x', \tau), \tag{77}$$

which corresponds to an ensemble averaged spatiotemporal bump riding on top of colored stationary noise. Instructively, partially coherent diffraction-free beams have been shown theoretically (Ponomarenko et al., 2007) and verified experimentally (Zhu et al., 2019) to possess the same spatial correlation structure.

At the same time, STOVs generated by light with reduced temporal coherence were also examined and realized in the laboratory (Mirando et al., 2021). An experimental setup for their generation is shown in Fig. 22. An amplified spontaneous emission light source based on a single-mode fiber was employed in the experiment. The distribution of light field was fully spatially coherent, corresponding to the fiber mode, but the source was spectrally broadband, implying a finite temporal coherence time. The STOV shape was shown to deviate significantly from a characteristic vortex ring as the source coherence time was reduced. The amplitude noise was found to spread in time, resulting in multiple peaks clearly visible in Fig. 23. Further, higher-order partially coherent STOVs were found to break up into fundamental vortices even at the source. In addition to the amplified spontaneous emission, noise-like pulse sources were also employed with similar results. A noise-like pulse source can be realized by a laser operating with multiple longitudinal modes that are partially correlated (not perfectly phase-locked).

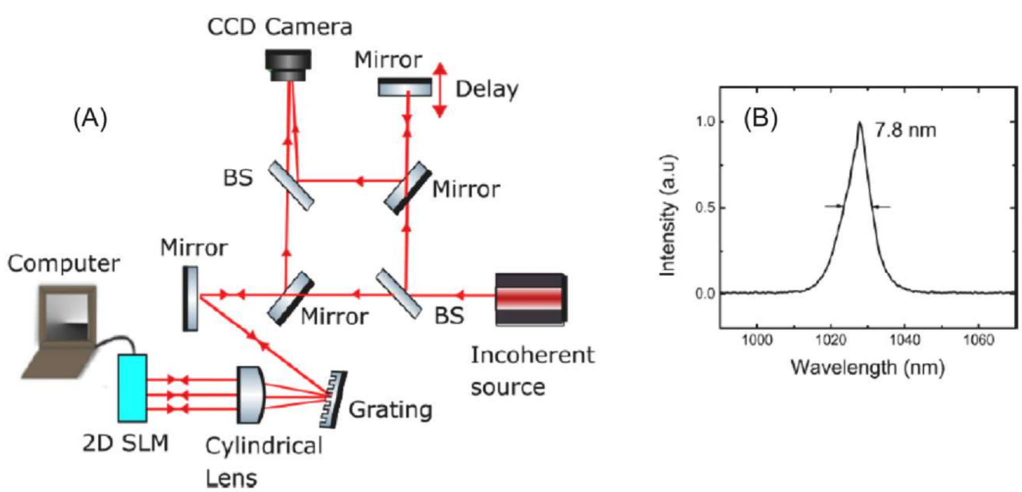

Fig. 22 (A) Schematic of the setup for partially coherent STOV generation. BS-beam splitter (B) Spectrum of the amplified spontaneous emission source *(B) Reproduced with permission from Mirando et al. (2021) ©Optica Publishing Group.*

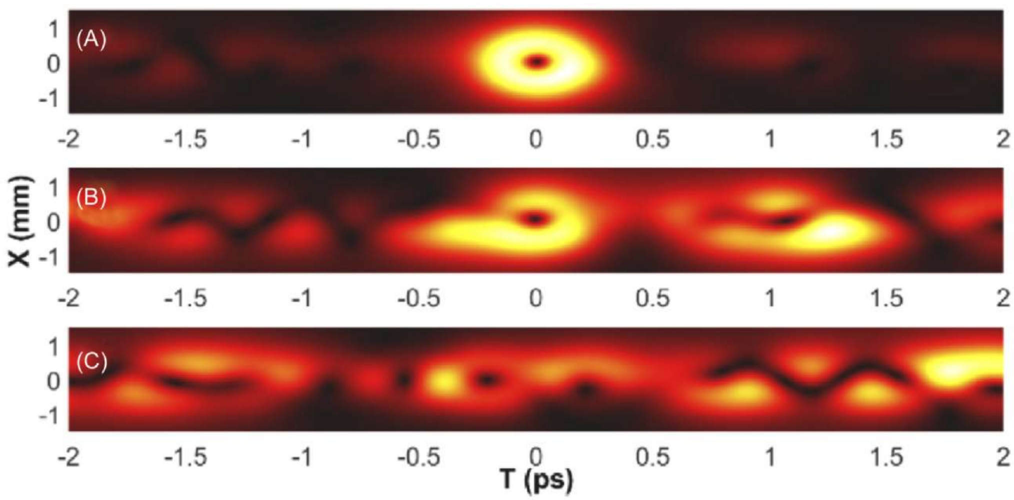

Fig. 23 Amplitude of partially coherent STOV with topological charge $l = 1$. Variance of each normal distribution is: (A) $\sigma^2 = 0.2\pi^2$, (B) $\sigma^2 = 0.5\pi^2$, (C) $\sigma^2 = \pi^2$. *(C) Reproduced with permission from Mirando et al. (2021) ©Optica Publishing Group.*

4.2 Spatiotemporal random surface plasmon polaritons

The celebrated surface plasmon polaritons (SPP) have attracted much attention in the context of nano-optics (Novotny & Hecht, 2012) as a ubiquitous class of surface electromagnetic waves (Chen et al., 2020). The interest in SPPs has led to the emergence of plasmonics as a separate subfield within nanophotonics (Maier, 2007) with numerous applications in science and engineering (Zayats et al., 2005; Zhang et al., 2012).

The SPPs are commonly treated as monochromatic, evanescent-like plane waves localized at an interface separating metal and dielectric media. Structured SPPs have also been considered, including Bessel (Bliokh et al., 2008; Lerman et al., 2009; Garcia-Ortiz et al., 2013), vortex (Gorodetski et al., 2008; Kim et al., 2010), long-range nondiffracting cosine-Gaussian (Lin et al., 2012), polarization-tunable (Lin et al., 2013), and self-accelerating Airy (Salandrino & Christodoulides, 2010; Minovich et al., 2011; Epstein & Arie, 2014) SPP wave packets. Nevertheless, most structured SPP fields explored to date have been either monochromatic, i.e., spatially and temporally coherent, or polychromatic but spatially completely coherent. Only lately have partially spatially and temporarily coherent SPPs been theoretically examined (Chen et al., 2020), motivated by recent advances in structuring spatial, spectral and polarization degrees of freedom (DoF) of polychromatic SPPs (Aberra Guebrou et al., 2012; Lavery et al., 2012; Wang et al., 2014). Specifically, the principle of plasmon coherence engineering was formulated that enabled sculpting SPPs of arbitrary degree of spatial and/or temporal coherence in a

Kretschmann configuration (Norrman et al., 2016). Applying said principle, a variety of partially coherent SPPs with structured amplitude, polarization and coherence properties have been theoretically explored, including axicon (Chen et al., 2018b), vortex (Chen et al., 2019), and lattice (Chen et al., 2018a) SPPs, as well as a multitude of tailored random SPPs generated from uncorrelated superpositions of coherent pseudo-modes (Mao et al., 2018).

We will now briefly describe the plasmon coherence engineering principle. We consider a polychromatic surface plasmon polariton wave packet (SPPWP) composed of TM-polarized (p-polarized) monochromatic SPPs coupled to a metal-dielectric interface in a Kretschmann configuration, shown in Fig. 24. The Kretschmann setup consists of a glass prism with a thin homogeneous, isotropic nonmagnetic film deposited on the horizontal surface of the prism. The metal-air interface is assumed to be the $z = 0$ plane of our coordinate system and all monochromatic SPPs of the SPPWP propagate in the positive x-direction. The dielectric is air. The electric field of such an SPP wave packet can be represented as (Norrman et al., 2016)

$$\mathbf{E}(\mathbf{r}, t) = \int_{\omega_-}^{\omega_+} d\omega\, E(\omega)\,\mathbf{e}_p(\omega)\,\mathrm{e}^{\mathrm{i}[\mathbf{k}(\omega)\cdot\mathbf{r}-\omega t]}, \tag{78}$$

where $\omega_\pm$ are the edges of the frequency bandwidth of the packet and $E(\omega)$ is a random complex spectral amplitude of a monochromatic SPP governed by the dispersion relation

$$\mathbf{k}(\omega) = k_x(\omega)\,\mathbf{e}_x + k_z(\omega)\,\mathbf{e}_z, \qquad \mathbf{e}_p(\omega) = [\mathbf{k}(\omega) \times \mathbf{e}_y]\,/\,|\mathbf{k}(\omega)|. \tag{79}$$

Here $\mathbf{e}_x$, $\mathbf{e}_y$ and $\mathbf{e}_z$ are Cartesian unit vectors and $\mathbf{e}_p$ is a unit polarization vector of the monochromatic component at frequency ω. Further, k_x and k_z are familiar wave vector components of a standard monochromatic SPP (Maier, 2007).

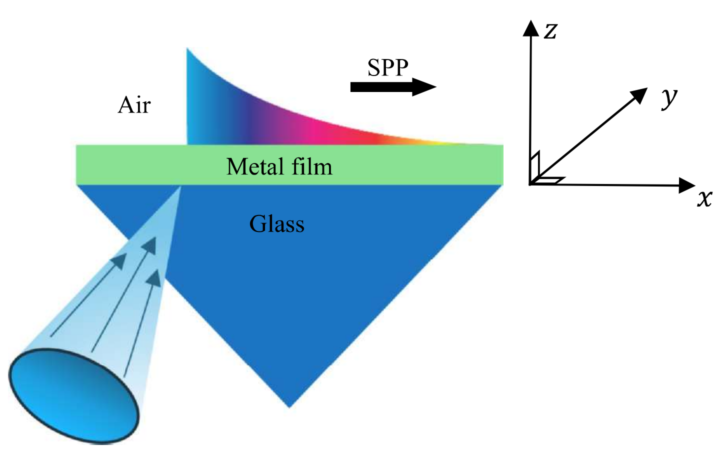

Fig. 24 Illustrating Kretschmann coupling geometry for partially coherent surface plasmon polariton excitation.

The second-order statistical properties of an ensemble of such SPPs in the space-frequency representation (Mandel & Wolf, 1995) are completely specified by the cross-spectral density tensor of the form

$$\mathbf{W}(\mathbf{r}_1, \omega_1; \mathbf{r}_2, \omega_2) = \langle \mathbf{E}^*(\mathbf{r}_1, \omega_1)\mathbf{E}^{\mathrm{T}}(\mathbf{r}_2, \omega_2)\rangle, \tag{80}$$

where the angle brackets and the superscript "T" denote ensemble averaging and matrix transposition, respectively. The cross-spectral density of any random SPP wave packet can be expressed as (Norrman et al., 2016)

$$\mathbf{W}(\mathbf{r}_1, \omega_1; \mathbf{r}_2, \omega_2) = W(\omega_1, \omega_2)\,\mathbf{e}_p^*(\omega_1)\,\mathbf{e}_p^{\mathrm{T}}(\omega_2)\,e^{i[\mathbf{k}(\omega_2)\cdot\mathbf{r}_2 - \mathbf{k}(\omega_1)\cdot\mathbf{r}_1]}, \tag{81}$$

in terms of the SPP spectral correlation function W defined as

$$W(\omega_1, \omega_2) = \langle E^*(\omega_1)E(\omega_2)\rangle. \tag{82}$$

The statistical properties of said wave packet in the space-time domain can then be described in terms of the mutual intensity tensor $\boldsymbol{\Gamma}$ related to the cross-spectral density tensor via a double Fourier transform as

$$\boldsymbol{\Gamma}(\mathbf{r}_1, t_1; \mathbf{r}_2, t_2) = \int_{\omega_-}^{\omega_+} d\omega_1 \int_{\omega_-}^{\omega_+} d\omega_2\, \mathbf{W}(\mathbf{r}_1, \omega_1; \mathbf{r}_2, \omega_2)\, e^{i(\omega_1 t_1 - \omega_2 t_2)}. \tag{83}$$

It follows from Eq. (81) that once the material parameters of the media and the source bandwidth are fixed, the spectral correlation function furnishes a flexible DoF to control all second-order statistical properties of SPPWP in either space-frequency, or space-time representation. The gist of plasmon coherence engineering is to tailor the coherence state of the excitation light source to customize W, and hence sculpt novel SPPWPs.

4.3 Partially coherent plasmon axicons, vortices and lattices

We now illustrate the power of plasmon coherence engineering paradigm by describing several classes of structured SPPWPs. To this end, we first consider a class of partially coherent SPPWPs whose field structure is reminiscent of a classic optical axicon (Jaroszewicz et al., 2005). We will refer to such SPPWPs as axiconic surface plasmon polariton (ASPP) fields (Chen et al., 2018b). To generate such structured SPPWPs, we can employ a coupling geometry similar to the standard Kretschmann setup of Fig. 24 with the caveat that the monochromatic SPPs, comprising the ASPP, propagate radially toward the center of a circle of radius a in the plane $z = 0$. The initial excitation positions of such elementary SPPs are distributed uniformly along the circumference of the circle as is shown in Fig. 25. Further, $\mathbf{r}_0(\theta)$ is a radius vector to the excitation point located on the circle in the direction specified by the azimuthal angle θ.

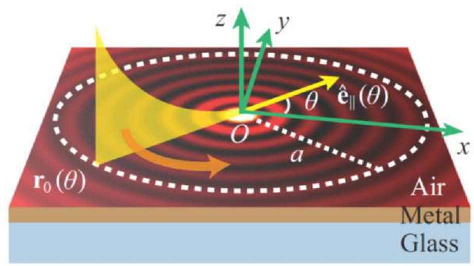

Fig. 25 Geometry of the ASPP field synthesis. One of the contributing SPPs, excited on the circle of radius *a* at the metal-air interface and propagating in the direction of $\hat{\mathbf{e}}_{||}(\theta)$, is explicitly displayed in the figure. Copyright (2018) by the American Physical Society. *Reprinted with permission from Chen et al. (2018b).*

The electric field of the ASPP wave packet can then be represented as

$$\mathbf{E}(\mathbf{r},\omega)=\int_0^{2\pi} d\theta\, E(\theta,\omega)\,\mathbf{e}_p(\theta,\omega)\,\mathrm{e}^{\mathrm{i}\mathbf{k}(\theta,\omega)\cdot[\mathbf{r}-\mathbf{r}_0(\theta)]}. \tag{84}$$

Here $E(\theta,\omega)$ is the complex angular-spectral amplitude of the monochromatic SPP at the excitation point, and the SPP wave vector components obey the equations

$$\mathbf{k}(\theta,\omega)=k_{||}(\omega)\mathbf{e}_{||}(\theta)+k_z(\omega)\mathbf{e}_z; \quad \mathbf{e}_p(\theta,\omega)=\mathbf{e}_k(\theta,\omega)\times[\mathbf{e}_z\times\mathbf{e}_{||}(\theta)], \tag{85}$$

where $\mathbf{e}_{||}(\theta)$ is a radial unit vector in polar coordinates in the interface plane $z=0$ and $\mathbf{e}_k(\theta,\omega)=\mathbf{k}(\theta,\omega)/|\mathbf{k}(\omega)|$. We note further that the magnitude $|\mathbf{k}(\omega)|$ of the wave vector $\mathbf{k}$ does not depend on the azimuthal angle θ on the circle. According to the plasmon coherence engineering paradigm, all second-order statistical properties of ASPPs are encapsulated in the following angular-spectral SPP correlation function:

$$W(\theta_1,\theta_2,\omega)=\langle E^*(\theta_1,\omega)E(\theta_2,\omega)\rangle. \tag{86}$$

To illustrate the ASPP design possibilities, we consider ASPPs generated on an AG/air interface with a coherent laser source with the carrier wavelength $\lambda=532$ nm. The individual SPPs are assumed to be perfectly angularly correlated, such that $W(\theta_1,\theta_2,\omega)=|E(\omega|^2=S_0(\omega)$, where $S_0(\omega)$ is a spectral density of each monochromatic SPP field. We show the ASPP spectrum in Fig. 26a. The latter has a typical axicon shape, similar to that of a plasmonic lens (Lerman et al., 2009), with a pronounced and tightly confined peak at the center of the circle. The central peak is induced by interference among the individual SPPs. As the angular correlations of the ASPP field are relaxed, the axicon peak at the center gradually fades away, giving way to a broad spectral intensity distribution over the entire interior of the circle (Chen et al., 2018b). However,

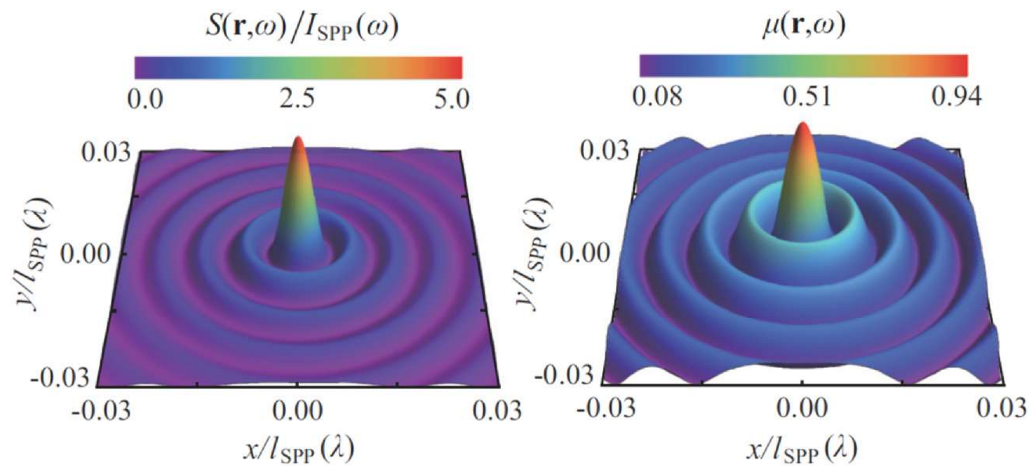

Fig. 26 (Left) Spectral density $S(\mathbf{r}, \omega)$ for the correlated ASPP field and (right) the degree of coherence $\mu(\mathbf{r}, \omega)$ for the uncorrelated ASPP field at an Ag-air interface for the free-space wavelength $\lambda = 632.8$ nm. In the left panel $I_{SPP}(\omega)$ is the initial SPP intensity and $a = l_{SPP}(\lambda)$, where a is the circle radius and $l_{SPP}(\lambda)$ is the SPP propagation length. In the right panel $\mu(\mathbf{r}, \omega)$ is independent of a, but $\sqrt{x^2 + y^2} \leq a$. The relative permittivity of Ag is from empirical data (Palik, 1998). *Reprinted with permission from Chen et al. (2018b). Copyright (2018) by the American Physical Society.*

as the angular correlations among the SPPs vanish altogether, $W(\theta_1, \theta_2, \omega) \propto \delta(\theta_1 - \theta_2)$ where $\delta(\ldots)$ is a Dirac delta function, the spectral oscillations disappear as well and the spectral peak shifts toward the circumference of the circle, that is, toward the SPP excitation positions. Remarkably, the axicon profile reemerges in the electromagnetic degree of coherence as is shown in Fig. 26B. This axicon shape revival has its origin in the phenomenon of statistical similarity of SPP fluctuations (Ponomarenko et al., 2005; Voipio et al., 2015), whereby even completely uncorrelated individual SPPs can produce a highly coherent ASPP field near the center of the circle.

It is also possible to sculpt partially coherent vortex SPPs (SPPV) upon endowing each individual SPP with a helical phase in the coupling configuration of Fig. 25. The excitation method is sketched in Fig. 27. To impart an OV to an SPP wave packet, the authors of (Chen et al., 2019) propose to focus a partially spatially coherent, radially polarized beam of circular cross-section onto a metal film. The source beam is assumed to carry the SAM s and OAM l per photon (in $\hbar$ units), respectively. We can then express the electric field of such an SPPV as (Chen et al., 2019)

$$\mathbf{E}(\mathbf{r}, \omega) = \int_0^{2\pi} d\theta \; E(\theta, \omega)\, \mathbf{e}_p(\theta, \omega)\, \mathrm{e}^{\mathrm{i}\mathbf{k}(\theta,\omega)\cdot[\mathbf{r}-\mathbf{r}_0(\theta)]}\, e^{im\theta}, \tag{87}$$

where $m = s + l$ is an integer and the other notations are the same as in Eq. (84).

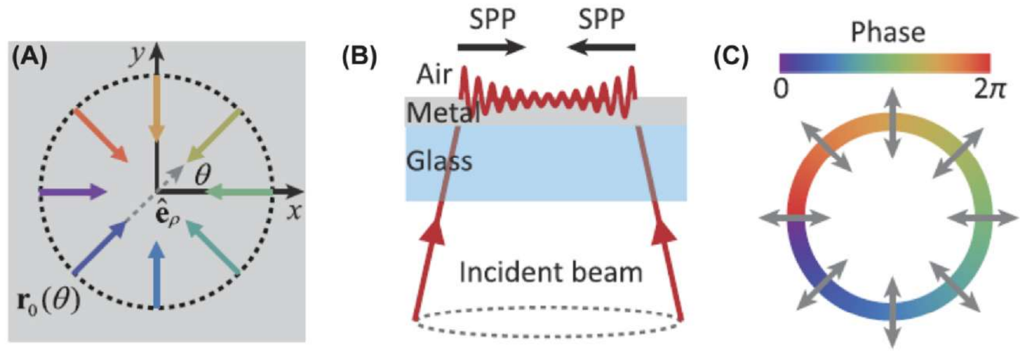

Fig. 27 (A) Synthesis of the partially coherent SPP vortex field by a continuum of radially propagating SPP modes with a prescribed initial phase profile and arbitrary correlations at a metal-air interface. The constituent SPPs are excited at points $\mathbf{r}_0(\theta)$ along a circular ring and propagate toward the ring center in the direction $\hat{\mathbf{e}}_\rho$, where $\theta \in [0, 2\pi)$ is the azimuth angle with respect to the *x*-axis. (B) A focused OAM carrying, radially polarized, and ring shaped, partially coherent incident beam illuminates the glass prism and metal slab structure to excite the radially propagating SPP modes shown in (A). (C) Illustration of the polarization state, beam shape, and phase distribution of a vortex mode with topological charge 1 of the incident partially coherent beam. *Reprinted with permission from Chen et al. (2021). Copyright (2021) by the American Physical Society.*

The source beam transfers SAM and OAM to an SPPV (Chen et al., 2021). Utilizing a canonical formalism in the space-frequency representation (Bliokh & Nori, 2015), we can determine the average OAM density of an ensemble of SPPVs at frequency ω as

$$\langle \mathbf{L}(\mathbf{r}, \omega) \rangle = \mathbf{r} \times \langle \mathbf{P}(\mathbf{r}, \omega) \rangle. \tag{88}$$

Here a canonical linear momentum $\mathbf{P}$ is defined as

$$\mathbf{P}(\mathbf{r}, \omega) = \frac{1}{4\omega}[\epsilon_0 \mathbf{E}^*(\mathbf{r}, \omega)\cdot[\nabla]\mathbf{E}(\mathbf{r}, \omega) + \mu_0 \mathbf{H}^*(\mathbf{r}, \omega)\cdot[\nabla]\mathbf{H}(\mathbf{r}, \omega)]. \tag{89}$$

in terms of the electric $\mathbf{E}$ and magnetic $\mathbf{H}$ fields of the ensemble representations. In Eq. (89), we employ a short-hand notation $\mathbf{A}\cdot[\nabla]\mathbf{B} = A_x \nabla B_x + A_y \nabla B_y + A_z \nabla B_z$. By the same token, the average SAM density can be evaluated as

$$\langle \mathbf{S}(\mathbf{r}, \omega) \rangle = \frac{1}{4\omega}[\epsilon_0 \langle \mathbf{E}^*(\mathbf{r}, \omega) \times \mathbf{E}(\mathbf{r}, \omega) \rangle + \mu_0 \langle \mathbf{H}^*(\mathbf{r}, \omega) \times \mathbf{H}(\mathbf{r}, \omega) \rangle]. \tag{90}$$

As the OAM of SPPVs is directed normal to the interface along which all individual SPPVs propagate, we can classify it as transverse. The SAM possesses both in-plane components—radial and azimuthal—and an out–of-plane one which is normal to the interface. It turns out that in-plane SAM components are caused by the SPPV electric field correlations.

Remarkably, though, the azimuthal SAM carries a component induced by the elementary SPPs comprising the surface plasmon polariton vortex field. At the same time, the out-of-plane SAM component exists thanks to the SPPV magnetic field correlations. This analysis (Chen et al., 2021) stresses the crucial role played by the spectral degree of electromagnetic coherence of the SPPV field in shaping its spin angular momentum distribution.

Yet another interesting option in the same circular coupling geometry of Fig. 25, is to structure SPPWPs with discrete spectrum. Such SPPWPs can be composed of a finite number N of SPPs uniformly distributed along the circle with $\mathbf{r}_{0n}$ representing the excitation position of the nth SPP located in the direction specified by the radial unit vector $\mathbf{e}_r^{(n)}$ and propagating toward the circle center. All individual SPPs are then assumed to be located at the vertices of a regular N-sided polygon with the azimuthal angle $\theta_n = 2\pi(n-1)/N$ corresponding to the nth SPP. We can then express the electric field of an ensemble realization of the resulting surface plasmon polariton lattice (SPPL) in air as (Chen et al., 2018a)

$$\mathbf{E}(\mathbf{r},\, \omega) = \sum_{n=1}^{N} \mathbf{e}_n E_n(\omega) e^{i\mathbf{k}_n\cdot(\mathbf{r}-\mathbf{r}_{0n})}, \tag{91}$$

where $E_n(\omega)$ is a (random) spectral amplitude of the nth SPP mode at the excitation point. The wave and unit polarization vectors of an individual SPPs read

$$\mathbf{k}_n = k_{\|}\mathbf{e}_r^{(n)} + k_z\mathbf{e}_z, \qquad \mathbf{e}_n = -[\mathbf{e}_z \times \mathbf{e}_r^{(n)}] \times \mathbf{k}_n/|\mathbf{k}_n| \tag{92}$$

In Fig. 28, we display the distribution of the spectral electromagnetic degree of coherence of an SPPL field composed of uncorrelated SPPs on an Ag/air interface at free-space wavelength $\lambda = 532$ nm. We can infer from the figure that in spite of lack of any interference among the SPPs, the electromagnetic degree of coherence has a lattice-like, subwavelength structure with rotational symmetry. We notice that the surface plasmon polariton lattices exhibit translational symmetry for small N, which transitons to rotational symmetry as N increases. Eventually surface plasmon polariton lattices transform to radially symmetric structures in the large N limit. This periodicity of coherence properties of plasmon lattices is reminiscent of *optical coherence lattices* that were previously explored theoretically in the context of paraxial statistical fields propagating in free space (Ma & Ponomarenko, 2014, 2015) and subsequently realized experimentally (Chen et al., 2016; Liang et al., 2021). The optical coherence lattices were also employed to generate high-quality arrays of Bessel beams (Liang et al., 2018).

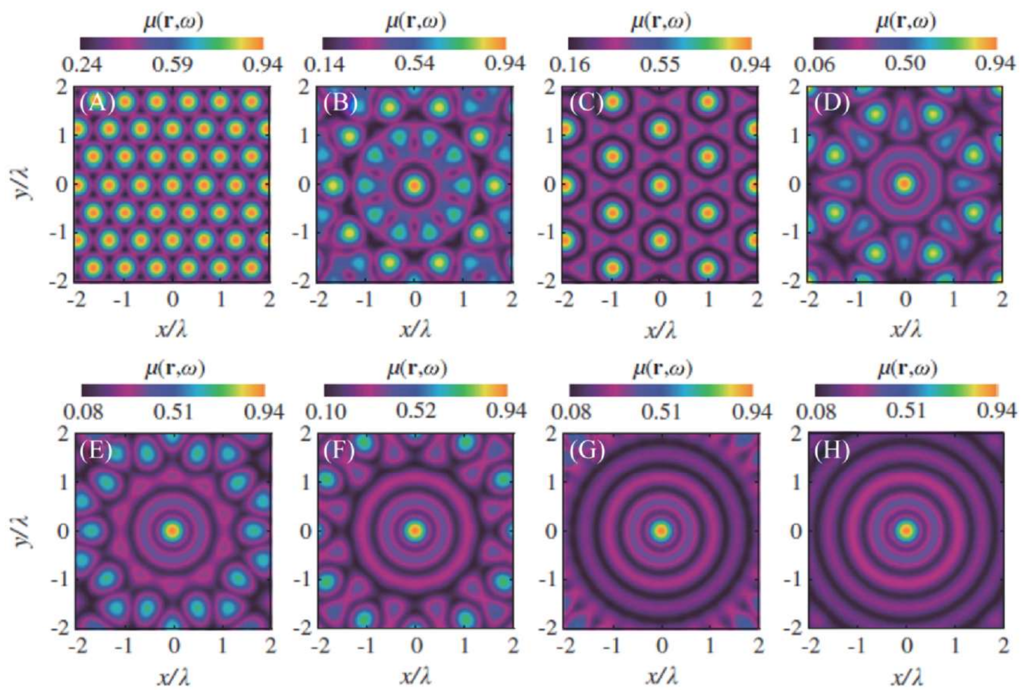

Fig. 28 Spatial behavior of the electromagnetic degree of coherence $\mu(\mathbf{r}, \omega)$ for uncorrelated surface plasmon polariton lattice fields at an Ag-air interface at the free-space wavelength $\lambda = 632.8$ nm with (A) $N = 3$, (B) $N = 5$, (C) $N = 6$, (D) $N = 8$, (E) $N = 10$, (F) $N = 12$, (G) $N = 15$, and (H) $N = 20$ SPP modes. Empirical data are used for Ag [33]. *(H) Reproduced with permission from Chen et al. (2018a) ©Optica Publishing Group.*

In the other extreme of fully correlated SPP modes, the *coherence lattices* disappear due to complete coherence, but, remarkably, the lattice structure reemerges in the context of *spectral density lattices* owing to the interference among the SPP modes (Chen et al., 2018a). The subwavelength periodicity of surface plasmon polariton lattice fields is attractive to a number of applications, including coherence lattices for controlled excitation of random molecule or quantum dot sets and nanoparticle trapping with spectral density or polarization lattices. In addition, partially coherent plasmon lattice fields can be employed to design highly flexible multi-particle nanoantenna array configurations which are robust against both surface defects and environmental fluctuations.

5. Applications, perspectives and outlook

5.1 Applications of structured space-time light

Shortly after the seminal discovery of a connection between optical vortices and longitudinal OAM (Allen et al., 1992b), the idea to employ light-induced torques, associated with the OAM, to rotate (tweeze) small neutral particles has been realized in the laboratory (Friese et al., 1998). However, the orbital angular momentum conservation stipulates that the vortex beams endowed with longitudinal OAM be only capable of rotating particles in a plane transverse to the beam propagation direction. A recently reported observation of the transfer of transverse spin and OAM to micro-particles has opened up new perspectives, though (Stilgoe et al., 2022). In particular, the STOVs with transverse OAM can rotate particles about an axis perpendicular to the STWP propagation direction, while STOVs with an adjustable OAM orientation enable arbitrary control over the particle rotation direction. Further, the transfer of a transverse OAM from light to matter is instrumental for producing sheer stress that makes it possible to study mechanotransduction within an individual material cell.

By the same token, STWPs carrying optical vortices offer greatly enhanced flexibility in OAM state sorting. The OAM sorting, which involves organizing the states of light according to their OAM structure, is crucial to numerous applications, enabling high-quality imaging, efficient optical communications, fast and accurate analog optical and quantum computing, as well as efficient and secure optical information processing. Engaging additional degrees of freedom associated with space-time coupling can dramatically enhance all these capabilities, but it comes at a cost. Rapid temporal dynamics of such STWPs presents a significant challenge for OAM state detecting and sorting. Nevertheless, potential payoffs make tackling this challenge worthwhile, creating an opportunity to open up new horizons in optical communications. For instance, the conversion among various structured spatiotemporal modes, such as Laguerre-Gaussian and Hermite-Gaussian wavepackets, can be utilized for radial and azimuthal quantum number recognition in real time. The latter has the potential to advance STOV applications that require fast temporal response, such as telecommunications and data encoding where quantum numbers of space-time Laguerre-Gaussian modes can play an important role.

Optical communications rely on transmission of information encoded into optical fields through either free-space or fiber optical communication channels. To boost the information capacity of any such channel, the bandwidth of an optical communication protocol must be maximized, usually through multiplexing available degrees of freedom of optical fields, such as intensity and phase profiles, wavelength and polarization. In the last few decades, much attention had been paid to incorporating longitudinal OAM into optical communication protocol. In this connection, the transverse, or even arbitrarily oriented OAM of STOVs brings a multitude of additional degrees of freedom to the fore. Moreover, higher-order spatiotemporal topological structures, such as hopfions or skyrmions with their numerous non-separable DoFs, can undoubtedly enrich the available toolkit to realize free-space optical communications. Recent advances in this direction include the discovery and demonstration of intricate spatiotemporal structures of increasingly complex topology through exploring the coupling between spatial and temporal degrees of freedom of light fields (Shen et al., 2023a, 2024b). Some higher-order knotted textures have been proposed as information carriers in optical networks (Larocque et al., 2020). Further, optical vortex knots and links were employed to implement high-capacity information coding (Kong et al., 2022).

At the same time, STWPs have emerged as an indispensable tool for harnessing entanglement of multiple quantum states which undergirds much of quantum information science. In this context, space-time coupling facilitates the generation of multiple entangled states with great efficiency and flexibility. For instance, fine-tuning the spatiotemporal properties of entangled photons brings about fidelity and range improvement of quantum information networks. Thus, the spatiotemporal degrees of freedom of light fields provide an essential capability for advancing quantum computing, quantum cryptography and quantum teleportation.

5.2 Perspectives and outlook

Over the last century, optical physics has enabled us to acquire unprecedented control over various degrees of freedom of light fields. The capability to generate optical fields with customizable spatiotemporal properties takes us one step closer to attain ultimate control of light fields, unlocking a unique potential of photonics for a dazzling array of applications from imaging and information transmission to classical and quantum optical networks. The concurrent rapid advances in nanomaterial fabrication and nanostructure engineering provide unprecedented opportunities to tailor light-matter interaction to a degree unimaginable to date.

Although impressive progress has been made in developing techniques for spatiotemporal wave packet sculpting, our current protocols for STWP generation largely rely on linear optics that utilizes bulky optical elements, such as spatial light modulators, to design STWPs in the space-frequency domain. The existing approaches suffer from low modulation efficiency and are not easily adaptable to minituarization. The recent development of metasurfaces and nanophotonics platforms with versatile multi-dimensional modulation capabilities carries promise for a new generation of protocols to produce STWPs with all spatial and temporal degrees of freedom mutually intertwined to form intricate spatiotemporal light structures for exploring fundamental aspects of light-matter interactions. By the same token, STWPs endowed with complex topological structures, such as optical hopfions, are expected to become instrumental to drastically enhance communication capacity of optical networks for image and information processing.

To date, STWPs are commonly generated and propagated in free space. The transmission of such wave packets through complex material media featuring dispersion and/or nonlinearity has only begun to be explored theoretically and yet to be investigated experimentally. Many fundamental questions remain open as to the interplay between the host medium dispersion and nonlinearity and space-time coupling of propagating light fields. We fully anticipate the dicovery of new physical phenomena here that will unlock the potential for novel applications.

The integration of the optics of space-time wave packets and quantum mechanics presents a new frontier, the exploration of which carries promise for breakthroughs in both our understanding of quantum physics of complex systems and applications of quantum optics. In particular, employing STWPs in the quantum optical domain can lead to the discovery of novel quantum states of light endowed with nontrivial topological properties. The latter can have their quantum coherence properties topologically protected against noise and decoherence effects. Further, mutual coupling of multiple DoFs of STWPs can enhance efficiency of quantum information processing as well as enable quantum entanglement across a multitude of DoFs. For instance, realizing quantum entanglement of OAM and SAM can showcase an entanglement distribution across multiple degrees of freedom within complex STWPs (Fickler et al., 2012; Stav et al., 2018).

Finally, the exploration of partially coherent STWPs has only just started. A recent discovery of classical phase-space entanglement of partially coherent light fields endowed with non-local twist phases, which vanish in the fully coherent limit (Ponomarenko, 2021), can open up new routes for quantum-like classical communications with such statistical STWPs that take advantage of the entanglement among their different DoFs, but do not require quantum nonlocality. Thus, employing classically entangled STWPs of partially coherent light in optical communications and optical computing (Liu et al., 2023; Li et al., 2024a; Cao et al., 2024) can help avoid pernicious decoherence problems that are inherent in fully quantum protocols.

In summary, theoretical and experimental advances in realizing optical wave packets with coupled spatiotemporal degrees of freedom have triggered the emergence of a thriving field of space-time optics. Although the field is in its infancy, we forecast the current rapid research progress to accelerate even further in the near future.

References

Aberra Guebrou, S., Laverdant, J., Symonds, C., Vignoli, S., & Bellessa, J. (2012). Spatial coherence properties of surface plasmon investigated by young's slit experiment. *Optics Letters, 37*, 2139–2141.

Abramochkin, E., Razueva, E., & Volostnikov, V. (2010). General astigmatic transform of Hermite–Laguerre–Gaussian beams. *Journal of the Optical Society of America A, 27*, 2506–2513.

Abramochkin, E., & Volostnikov, V. (1991). Beam transformations and nontransformed beams. *Optics Communications, 83*, 123–135.

Abramochkin, E., & Volostnikov, V. (2004). Generalized Gaussian beams. *Journal of Optics A: Pure and Applied Optics, 6*, S157.

Abramochkin, E., & Volostnikov, V. (2010). Generalized hermite-laguerre-gauss beams. *Physics of Wave Phenomena, 18*, 14–22.

Agrawal, G. P. (2023). *Physics and engineering of Graded-Index media*. Cambridge University Press.

Allen, L., Beijersbergen, M. W., Spreeuw, R., & Woerdman, J. (1992a). Orbital angular momentum of light and the transformation of laguerre-Gaussian laser modes. *Physical Review A, 45*, 8185.

Allen, L., Beijersbergen, M. W., Spreeuw, R., & Woerdman, J. (1992b). Orbital angular momentum of light and the transformation of laguerre-Gaussian laser modes. *Physical Review A, 45*, 8185.

Allende Motz, A. M., Yessenov, M., Bhaduri, B., & Abouraddy, A. F. (2021). Refraction of space-time wave packets: ii. Experiments at normal incidence. *Journal of the Optical Society of America A, 38*, 1450–1461.

Amiri, P., Rasouli, S., Hebri, D., & Ponomarenko, S. A. (2025). Talbot-effect-based multiplication of laguerre–Gaussian beams with non-zero radial indices: From theory to experimental realization. *Optics Communications, 574*, 131203.

Azaña, J., & Muriel, M. A. (1999). Temporal talbot effect in fiber gratings and its applications. *Applied Optics, 38*, 6700–6704.

Babaev, E., Faddeev, L. D., & Niemi, A. J. (2002). Hidden symmetry and knot solitons in a charged two-condensate bose system. *Physical Review B, 65*, 100512.

Baez, J. C., & Muniain, J. P. (1994). *Gauge fields, knots and gravity Vol. 4*. World Scientific Publishing Company.

Balazs, M., & Berry, M. (1979). Nonspreading wave packets. *American Journal of Physics, 4*, 264–267.

Bandres, M. A., & Gutiérrez-Vega, J. C. (2004). Ince–Gaussian beams. *Optics Letters, 29*, 144–146.

Bandres, M. A., Gutiérrez-Vega, J. C., & Chávez-Cerda, S. (2004). Parabolic nondiffracting optical wave fields. *Optics Letters, 29*, 44–46.

Battye, R. A., & Sutcliffe, P. M. (1998). Knots as stable soliton solutions in a three-dimensional classical field theory. *Physical Review Letters, 81*, 4798.

Bekshaev, A. (2024). Spatio-temporal optical vortices: Principles of description and basic properties. *arXiv Preprint* arXiv:2403.01751.

Belanger, P. (1984). Packetlike solutions of the homogeneous-wave equation. *Journal of the Optical Society of America A, 1*, 723–724.

Berger, M. A. (1999). Introduction to magnetic helicity. *Plasma Physics and Controlled Fusion, 41*, B167.

Berkhout, G. C., Lavery, M. P., Courtial, J., Beijersbergen, M. W., & Padgett, M. J. (2010). Efficient sorting of orbital angular momentum states of light. *Physical Review Letters, 105*, 153601.

Berry, M. (2001). Knotted zeros in the quantum states of hydrogen. *Foundations of Physics, 31*, 659–667.

Berry, M. V., & Dennis, M. R. (2001). Knotted and linked phase singularities in monochromatic waves. *Proceedings of the Royal Society of London. Series A: Mathematical, Physical and Engineering Sciences, 457*, 2251–2263.

Berry, M. V., & Klein, S. (1996). Integer, fractional and fractal talbot effects. *Journal of Modern Optics, 43*, 2139–2164.

Bhaduri, B., Yessenov, M., & Abouraddy, A. F. (2020). Anomalous refraction of optical spacetime wave packets. *Nature Photonics, 14*, 416–421.

Bhaduri, B., Yessenov, M., Reyes, D., Pena, J., Meem, M., Fairchild, S. R., ... Abouraddy, A. F. (2019). Broadband space-time wave packets propagating 70 m. *Optics Letters, 44*, 2073–2076.

Bialynicki-Birula, I., & Bialynicka-Birula, Z. (2003). Vortex lines of the electromagnetic field. *Physical Review A, 67*, 062114.

Bliokh, K. Y. (2021). Spatiotemporal vortex pulses: Angular momenta and spin-orbit interaction. *Physical Review Letters, 126*, 243601.

Bliokh, K. Y., & Aiello, A. (2013). Goos–hänchen and imbert–fedorov beam shifts: An overview. *Journal of Optics, 15*, 014001.

Bliokh, K. Y., Gorodetski, Y., Kleiner, V., & Hasman, E. (2008). Coriolis effect in optics: Unified geometric phase and spin-hall effect. *Physical Review Letters, 101*, 030404.

Bliokh, K. Y., Karimi, E., Padgett, M. J., Alonso, M. A., Dennis, M. R., Dudley, A., Forbes, A., Zahedpour, S., Hancock, S. W., Milchberg, H. M., et al. (2023). Roadmap on structured waves. *Journal of Optics, 25*, 103001.

Bliokh, K. Y., & Nori, F. (2012). Spatiotemporal vortex beams and angular momentum. *Physical Review A—Atomic, Molecular, and Optical Physics, 86*, 033824.

Bliokh, K. Y., & Nori, F. (2015). Transverse and longitudinal angular momenta of light. *Physics Reports, 592*, 1–38.

Broky, J., Siviloglou, G. A., Dogariu, A., & Christodoulides, D. N. (2008). Self-healing properties of optical airy beams. *Optics Express, 16*, 12880–12891.

Bryngdahl, O. (1974). Geometrical transformations in optics. *Journal of the Optical Society of America, 64*, 1092–1099.

Buono, W. T., & Forbes, A. (2022). Nonlinear optics with structured light. *Opto-Electronic Advances, 5*, 210174–1.

Cai, Y., Chen, Y., Yu, J., Liu, X., & Liu, L. (2017). Generation of partially coherent beams. *Progress in Optics, 62*, 157–223.

Cao, Q., Chen, J., Lu, K., Wan, C., Chong, A., & Zhan, Q. (2022). Non-spreading bessel spatiotemporal optical vortices. *Science Bulletin, 67*, 133–140.

Cao, T., Jin, S., Chen, Q., Ma, P., Ponomarenko, S. A., Cai, Y., ... Liu, J. (2025). Diffraction-free partially coherent pearcey beam. *Optics Express, 33*, 1827–1835.

Cao, T., Liu, X., Chen, Q., Ponomarenko, S. A., Cai, Y., & Liang, C. (2024). Prime number factorization and degree of coherence of speckled light beams. *Optics Letters, 49*, 5232–5235.

Céspedes Vicente, O., & Caloz, C. (2021). Bessel beams: A unified and extended perspective. *Optica, 8*, 451–457.

Chandrasekhar, S., & Kendall, P. C. (1957). On force-free magnetic fields. *Astrophysical Journal, 126*, 457.
Chen, W., Zhang, W., Liu, Y., Meng, F.-C., Dudley, J. M., & Lu, Y.-Q. (2022). Time diffraction-free transverse orbital angular momentum beams. *Nature Communications, 13*, 4021.
Chen, Y., Norrman, A., Ponomarenko, S. A., & Friberg, A. T. (2018a). Coherence lattices in surface plasmon polariton fields. *Optics Letters, 43*, 3429–3432.
Chen, Y., Norrman, A., Ponomarenko, S. A., & Friberg, A. T. (2018b). Partially coherent axiconic surface plasmon polariton fields. *Physical Review A, 97*, 041801.
Chen, Y., Norrman, A., Ponomarenko, S. A., & Friberg, A. T. (2019). Partially coherent surface plasmon polariton vortex fields. *Physical Review A, 100*, 053833.
Chen, Y., Norrman, A., Ponomarenko, S. A., & Friberg, A. T. (2020). *Optical coherence and electromagnetic surface waves. Progress in Optics*. Elsevier 105–172 volume 65.
Chen, Y., Norrman, A., Ponomarenko, S. A., & Friberg, A. T. (2021). Spin density in partially coherent surface-plasmon-polariton vortex fields. *Physical Review A, 103*, 063511.
Chen, Y., Ponomarenko, S. A., & Cai, Y. (2016). Experimental generation of optical coherence lattices. *Applied Physics Letters,* 109.
Chen, Y., Ponomarenko, S. A., & Cai, Y. (2017). Self-steering partially coherent beams. *Scientific Reports, 7*, 39957.
Chong, A., Renninger, W. H., Christodoulides, D. N., & Wise, F. W. (2010). Airy–bessel wave packets as versatile linear light bullets. *Nature Photonics, 4*, 103–106.
Chong, A., Wan, C., Chen, J., & Zhan, Q. (2020). Generation of spatiotemporal optical vortices with controllable transverse orbital angular momentum. *Nature Photonics, 14*, 350–354.
Conti, C., Trillo, S., DiTrapani, P., Valiulis, G., Piskarskas, A., Jedrkiewicz, O., & Trull, J. (2003). Nonlinear electromagnetic x waves. *Physical Review Letters, 90*, 170406.
Cundiff, S. T., & Weiner, A. M. (2010). Optical arbitrary waveform generation. *Nature Photonics, 4*, 760–766.
Dennis, M. R., King, R. P., Jack, B., O'holleran, K., & Padgett, M. J. (2010). Isolated optical vortex knots. *Nature Physics, 6*, 118–121.
Ding, C., Horoshko, D., Korotkova, O., Jing, C., Qi, X., & Pan, L. (2022). Source coherence-induced control of spatiotemporal coherency vortices. *Optics Express, 30*, 19871–19888.
Ding, C., Liang, C., Horoshko, D., Korotkova, O., Pan, L., & Liu, Z. (2023). Method for generating spatiotemporal coherency vortices and spatiotemporal dislocation curves. *Optics Express, 32*, 609–624.
Durnin, J. (1987). Exact solutions for nondiffracting beams. I. the scalar theory. *Journal of the Optical Society of America A, 4*, 651–654.
Durnin, J., Miceli, J., Jr, & Eberly, J. H. (1987). Diffraction-free beams. *Physical Review Letters, 58*, 1499.
Efremidis, N. K., Chen, Z., Segev, M., & Christodoulides, D. N. (2019). Airy beams and accelerating waves: An overview of recent advances. *Optica, 6*, 686–701.
Epstein, I., & Arie, A. (2014). Arbitrary bending plasmonic light waves. *Physical Review Letters, 112*, 023903.
Essex, E. (1977). Hertz vector potentials of electromagnetic theory. *American Journal of Physics, 45*, 1099–1101.
Faddeev, L., & Niemi, A. J. (1997). Stable knot-like structures in classical field theory. *Nature, 387*, 58–61.
Fan, H., Cao, Q., Liu, X., Chong, A., & Zhan, Q. (2025). Perfect spatiotemporal optical vortices. *arXiv Preprint* arXiv:2501.11426.

Fickler, R., Lapkiewicz, R., Plick, W. N., Krenn, M., Schaeff, C., Ramelow, S., & Zeilinger, A. (2012). Quantum entanglement of high angular momenta. *Science, 338*, 640–643.

Forbes, A. (2019). Structured light from lasers. *Laser & Photonics Reviews, 13*, 1900140.

Forbes, A., De Oliveira, M., & Dennis, M. R. (2021). Structured light. *Nature Photonics, 15*, 253–262.

Friese, M. E., Nieminen, T. A., Heckenberg, N. R., & Rubinsztein-Dunlop, H. (1998). Optical alignment and spinning of laser-trapped microscopic particles. *Nature, 394*, 348–350.

Garcia-Ortiz, C. E., Coello, V., Han, Z., & Bozhevolnyi, S. I. (2013). Generation of diffraction-free plasmonic beams with one-dimensional bessel profiles. *Optics Letters, 38*, 905–907.

Gori, F. (1980). Collett-wolf sources and multimode lasers. *Optics Communications, 34*, 301–305.

Gori, F., Guattari, G., & Padovani, C. (1987). Modal expansion for j0-correlated schell-model sources. *Optics Communications, 64*, 311–316.

Gorodetski, Y., Niv, A., Kleiner, V., & Hasman, E. (2008). Observation of the spin-based plasmonic effect in nanoscale structures. *Physical Review Letters, 101*, 043903.

Guérineau, N., Harchaoui, B., & Primot, J. (2000). Talbot experiment re-examined: Demonstration of an achromatic and continuous self-imaging regime. *Optics Communications, 180*, 199–203.

Gutiérrez-Vega, J. C., Iturbe-Castillo, M., & Chávez-Cerda, S. (2000). Alternative formulation for invariant optical fields: Mathieu beams. *Optics Letters, 25*, 1493–1495.

Hajati, M., Sieben, V., & Ponomarenko, S. A. (2021). Airy beams on incoherent background. *Optics Letters, 46*, 3961–3964.

Hall, L. A., & Abouraddy, A. F. (2021). Free-space group-velocity dispersion induced in space-time wave packets by v-shaped spectra. *Physical Review A, 104*, 013505.

Hall, L. A., Ponomarenko, S., & Abouraddy, A. F. (2021a). Temporal talbot effect in free space. *Optics Letters, 46*, 3107–3110.

Hall, L. A., Yessenov, M., & Abouraddy, A. F. (2022). Arbitrarily accelerating space-time wave packets. *Optics Letters, 47*, 694–697.

Hall, L. A., Yessenov, M., Ponomarenko, S. A., & Abouraddy, A. F. (2021b). The space–time talbot effect. *APL Photonics, 6*.

Hancock, S., Zahedpour, S., Goffin, A., & Milchberg, H. (2019). Free-space propagation of spatiotemporal optical vortices. *Optica, 6*, 1547–1553.

Hancock, S., Zahedpour, S., & Milchberg, H. (2021). Mode structure and orbital angular momentum of spatiotemporal optical vortex pulses. *Physical Review Letters, 127*, 193901.

He, C., Shen, Y., & Forbes, A. (2022). Towards higher-dimensional structured light. *Light: Science & Applications, 11*, 205.

Hellwarth, R., & Nouchi, P. (1996). Focused one-cycle electromagnetic pulses. *Physical Review E, 54*, 889.

Hossack, W., Darling, A., & Dahdouh, A. (1987). Coordinate transformations with multiple computer-generated optical elements. *Journal of Modern Optics, 34*, 1235–1250.

Huang, S., Wang, P., Shen, X., Liu, J., & Li, R. (2022). Diffraction properties of light with transverse orbital angular momentum. *Optica, 9*, 469–472.

Huang, Y.-W., Chen, W. T., Wu, P. C., Fedotov, V. A., Zheludev, N. I., & Tsai, D. P. (2013). Toroidal lasing spaser. *Scientific reports, 3*, 1237.

Hyde, M. W., IV (2020). Twisted space-frequency and space-time partially coherent beams. *Scientific Reports, 10*, 12443.

Hyde, M. W., IV (2024). Twisted spatiotemporal optical vortex beams in dispersive media. *Optics Communications, 566*, 130682.

Hyde, M. W., IV, Korotkova, O., & Spencer, M. F. (2023). Partially coherent sources whose coherent modes are spatiotemporal optical vortex beams. *Journal of Optics, 25*, 035606.
Hyde, M. W., IV, & Porras, M. A. (2023). Propagation of spatiotemporal optical vortex beams in linear, second-order dispersive media. *Physical Review A, 108*, 013519.
Irvine, W. T., & Bouwmeester, D. (2008). Linked and knotted beams of light. *Nature Physics, 4*, 716–720.
Jackson, J. D. (2021). *Classical electrodynamics*. John Wiley & Sons.
Jannson, T., & Jannson, J. (1981). Temporal self-imaging effect in single-mode fibers. *Journal of the Optical Society of America, 71*, 1373–1376.
Jaroszewicz, Z., Burvall, A., & Friberg, A. T. (2005). Axicon–the most important optical element. *Optics and Photonics News, 16*, 34–39.
Jhajj, N., Larkin, I., Rosenthal, E., Zahedpour, S., Wahlstrand, J., & Milchberg, H. (2016). Spatiotemporal optical vortices. *Physical Review X, 6*, 031037.
Jiang, Z., Huang, C.-B., Leaird, D. E., & Weiner, A. M. (2007). Optical arbitrary waveform processing of more than 100 spectral comb lines. *Nature Photonics, 1*, 463–467.
Kamien, R. D. (2002). The geometry of soft materials: A primer. *Reviews of Modern Physics, 74*, 953.
Kelvin, L. (1867). On vortex atoms. *Proceedings of Royal Society Edinburgh, Vol. 6*, 94–105.
Khonina, S. N., Kazanskiy, N. L., Karpeev, S. V., & Butt, M. A. (2020). Bessel beam: Significance and applications—a progressive review. *Micromachines, 11*, 997.
Kilner, P. J., Yang, G.-Z., Wilkes, A. J., Mohiaddin, R. H., Firmin, D. N., & Yacoub, M. H. (2000). Asymmetric redirection of flow through the heart. *Nature, 404*, 759–761.
Kim, H., Park, J., Cho, S.-W., Lee, S.-Y., Kang, M., & Lee, B. (2010). Synthesis and dynamic switching of surface plasmon vortices with plasmonic vortex lens. *Nano Letters, 10*, 529–536.
Kondakci, H. E., & Abouraddy, A. F. (2017). Diffraction-free space–time light sheets. *Nature Photonics, 11*, 733–740.
Kondakci, H. E., & Abouraddy, A. F. (2019). Optical space-time wave packets having arbitrary group velocities in free space. *Nature Communications, 10*, 929.
Kong, L.-J., Zhang, W., Li, P., Guo, X., Zhang, J., Zhang, F., ... Zhang, X. (2022). High capacity topological coding based on nested vortex knots and links. *Nature Communications, 13*, 2705.
Kotlyar, V., & Kovalev, A. (2014). Hermite–Gaussian modal laser beams with orbital angular momentum. *Journal of the Optical Society of America A, 31*, 274–282.
Lancis, J., Sicre, E., Pons, A., & Saavedra, G. (1995). Achromatic White-light self-imaging phenomenon: An approach using the wigner distribution function. *Journal of Modern Optics, 42*, 425–434.
Larocque, H., D'Errico, A., Ferrer-Garcia, M. F., Carmi, A., Cohen, E., & Karimi, E. (2020). Optical framed knots as information carriers. *Nature Communications, 11*, 5119.
Lavery, M. P., Robertson, D. J., Berkhout, G. C., Love, G. D., Padgett, M. J., & Courtial, J. (2012). Refractive elements for the measurement of the orbital angular momentum of a single photon. *Optics Express, 20*, 2110–2115.
Le, M., Hine, G., Goffin, A., Palastro, J., & Milchberg, H. (2024). Self-focused pulse propagation is mediated by spatiotemporal optical vortices. *arXiv Preprint* arXiv:2403.04669.
Leach, J., Dennis, M. R., Courtial, J., & Padgett, M. J. (2004). Knotted threads of darkness. *Nature, 432*, 165.
Lerman, G. M., Yanai, A., & Levy, U. (2009). Demonstration of nanofocusing by the use of plasmonic lens illuminated with radially polarized light. *Nano Letters, 9*, 2139–2143.
Li, X., Liu, X., Wu, Q., Zeng, J., Cai, Y., Ponomarenko, S. A., & Liang, C. (2024a). Prime number factorization with light beams carrying orbital angular momentum. *APL Photonics, 9*.

Li, X., Wang, Y., Liu, X., Ma, Y., Cai, Y., Ponomarenko, S. A., & Liu, X. (2024b). Deep learning and random light structuring ensure robust free-space communications. *Applied Physics Letters,* 124.
Li, Z., Gu, Y., & Kawanaka, J. (2021). Reciprocating propagation of laser pulse intensity in free space. *Communications Physics, 4*, 87.
Li, Z., & Kawanaka, J. (2020a). Optical wave-packet with nearly-programmable group velocities. *Communications Physics, 3*, 211.
Li, Z., & Kawanaka, J. (2020b). Velocity and acceleration freely tunable straight-line propagation light bullet. *Scientific Reports, 10*, 11481.
Liang, C., Liu, X., Xu, Z., Wang, F., Wen, W., Ponomarenko, S. A., ... Ma, P. (2021). Perfect optical coherence lattices. *Applied Physics Letters,* 119.
Liang, C., Zhu, X., Mi, C., Peng, X., Wang, F., Cai, Y., & Ponomarenko, S. A. (2018). High-quality partially coherent bessel beam array generation. *Optics Letters, 43*, 3188–3191.
Lim, T., & Nickels, T. (1992). Instability and reconnection in the head-on collision of two vortex rings. *Nature, 357*, 225–227.
Lin, J., Dellinger, J., Genevet, P., Cluzel, B., De Fornel, F., & Capasso, F. (2012). Cosine-Gauss plasmon beam: a localized long-range nondiffracting surface wave. *Physical Review Letters, 109*, 093904.
Lin, J., Mueller, J. P. B., Wang, Q., Yuan, G., Antoniou, N., Yuan, X.-C., & Capasso, F. (2013). Polarization-controlled tunable directional coupling of surface plasmon polaritons. *Science, 340*, 331–334.
Liu, X., Cao, Q., & Zhan, Q. (2024a). Spatiotemporal optical wavepackets: From concepts to applications. *Photonics Insights, 3*, R08.
Liu, X., Cao, Q., Zhang, N., Chong, A., Cai, Y., & Zhan, Q. (2024b). Spatiotemporal optical vortices with controllable radial and azimuthal quantum numbers. *Nature Communications, 15*, 5435.
Liu, X., Li, X., Ponomarenko, S. A., Wang, F., Peng, X., Cai, Y., & Liang, C. (2025). Unlocking secure optical multiplexing with spatially incoherent light. *Laser & Photonics Reviews*, 2401534.
Liu, X., Liang, C., Cai, Y., & Ponomarenko, S. A. (2023). Axial correlation revivals and number factorization with structured random waves. *Physical Review Applied, 20*, L021004.
Longhi, S. (2004). Gaussian pulsed beams with arbitrary speed. *Optics Express, 12*, 935–940.
Lotti, A., Couairon, A., Faccio, D., & Di Trapani, P. (2010). Energy-flux characterization of conical and space-time coupled wave packets. *Physical Review A, 81*, 023810.
Ma, L., & Ponomarenko, S. A. (2014). Optical coherence gratings and lattices. *Optics Letters, 39*, 6656–6659.
Ma, L., & Ponomarenko, S. A. (2015). Free-space propagation of optical coherence lattices and periodicity reciprocity. *Optics Express, 23*, 1848–1856.
Maier, S. A. (2007). *Plasmonics: Fundamentals and applications*. Berlin: Springer.
Mandel, L., & Wolf, E. (1995). *Optical coherence and quantum optics*. Cambridge University Press.
Mao, H., Chen, Y., Liang, C., Chen, L., Cai, Y., & Ponomarenko, S. A. (2019). Self-steering partially coherent vector beams. *Optics Express, 27*, 14353–14368.
Mao, H., Chen, Y., Ponomarenko, S. A., & Friberg, A. T. (2018). Coherent pseudo-mode representation of partially coherent surface plasmon polaritons. *Optics Letters, 43*, 1395–1398.
Martínez-Herrero, R., Mejías, P., & Gori, F. (2009). Genuine cross-spectral densities and pseudo-modal expansions. *Optics Letters, 34*, 1399–1401.
Mazanov, M., Sugic, D., Alonso, M. A., Nori, F., & Bliokh, K. Y. (2022). Transverse shifts and time delays of spatiotemporal vortex pulses reflected and refracted at a planar interface. *Nanophotonics, 11*, 737–744.

Minovich, A., Klein, A. E., Janunts, N., Pertsch, T., Neshev, D. N., & Kivshar, Y. S. (2011). Generation and near-field imaging of airy surface plasmons. *Physical Review Letters, 107*, 116802.
Mirando, A., Zang, Y., Zhan, Q., & Chong, A. (2021). Generation of spatiotemporal optical vortices with partial temporal coherence. *Optics Express, 29*, 30426–30435.
Miroshnichenko, A. E., Evlyukhin, A. B., Yu, Y. F., Bakker, R. M., Chipouline, A., Kuznetsov, A. I., ... Kivshar, Y. S. (2015). Nonradiating anapole modes in dielectric nanoparticles. *Nature Communications, 6*, 8069.
Moffatt, H. K. (1969). The degree of knottedness of tangled vortex lines. *Journal of Fluid Mechanics, 35*, 117–129.
Montgomery, W. D. (1967). Self-imaging objects of infinite aperture. *Journalof the Optical Society of America, 57*, 772–778.
Moses, H. E. (1971). Eigenfunctions of the curl operator, rotationally invariant helmholtz theorem, and applications to electromagnetic theory and fluid mechanics. *SIAM Journal on Applied Mathematics, 21*, 114–144.
Moshinsky, M. (1952). Diffraction in time. *Physical Review, 88*, 625.
Nemirovskii, S. K. (2013). Quantum turbulence: Theoretical and numerical problems. *Physics Reports, 524*, 85–202.
Norrman, A., Ponomarenko, S. A., & Friberg, A. T. (2016). Partially coherent surface plasmon polaritons. *Europhysics Letters, 116*, 64001.
Novotny, L., & Hecht, B. (2012). *Principles of nano-optics* (2nd ed.). Cambridge: Cambridge University Press.
Nye, J. F., & Berry, M. V. (1974). Dislocations in wave trains. *Proceedings of the Royal Society of London. A. Mathematical and Physical Sciences, 336*, 165–190.
Packross, B., Eschbach, R., & Bryngdahl, O. (1984). Achromatization of the self-imaging (talbot) effect. *Optics Communications, 50*, 205–209.
Padgett, M. J. (2017). Orbital angular momentum 25 years on. *Optics Express, 25*, 11265–11274.
Palik, E. D. (1998). *Handbook of optical constants of solids Vol. 3*. Academic Press.
Patorski, K. (1989). The self-imaging phenomenon and its applications. *Progress in Optics, 27*, 1–108.
Peng, D., Huang, Z., Liu, Y., Chen, Y., Wang, F., Ponomarenko, S. A., & Cai, Y. (2021). Optical coherence encryption with structured random light. *PhotoniX, 2*, 1–15.
Plick, W. N., & Krenn, M. (2015). Physical meaning of the radial index of laguerre-gauss beams. *Physical Review A, 92*, 063841.
Ponomarenko, S. A. (2001a). A class of partially coherent beams carrying optical vortices. *Journal of the Optical Society of America A, 18*, 150–156.
Ponomarenko, S. A. (2001b). Twisted Gaussian schell-model solitons. *Physical Review E, 64*, 036618.
Ponomarenko, S. A. (2011). Complex Gaussian representation of statistical pulses. *Optics Express, 19*, 17086–17091.
Ponomarenko, S. A. (2015). Self-imaging of partially coherent light in graded-index media. *Optics Letters, 40*, 566–568.
Ponomarenko, S. A. (2021). Twist phase and classical entanglement of partially coherent light. *Optics Letters, 46*, 5958–5961.
Ponomarenko, S. A., & Hebri, D. (2024). Perfect space–time vortices. *Optics Letters, 49*, 4322–4325.
Ponomarenko, S. A., Huang, W., & Cada, M. (2007). Dark and antidark diffraction-free beams. *Optics Letters, 32*, 2508–2510.
Ponomarenko, S. A., Roychowdhury, H., & Wolf, E. (2005). Physical significance of complete spatial coherence of optical fields. *Physics Letters A, 345*, 10–12.

Ponomarenko, S. A., Zhang, J., & Agrawal, G. P. (2022). Goos-hänchen shift at a temporal boundary. *Physical Review A, 106*, L061501.
Porras, M. A. (2017). Gaussian beams diffracting in time. *Optics Letters, 42*, 4679–4682.
Porras, M. A. (2023). Propagation of higher-order spatiotemporal vortices. *Optics Letters, 48*, 367–370.
Porras, M. A., & Di Trapani, P. (2004). Localized and stationary light wave modes in dispersive media. *Physical Review E, 69*, 066606.
Porras, M. A., & Jolly, S. W. (2023). Control of vortex orientation of ultrashort optical pulses using a spatial chirp. *Optics Letters, 48*, 6448–6451.
Porras, M. A., Trillo, S., Conti, C., & Di Trapani, P. (2003). Paraxial envelope x waves. *Optics Letters, 28*, 1090–1092.
Qin, C., Wang, S., Wang, B., Hu, X., Liu, C., Li, Y., ... Lu, P. (2024). Temporal goos-hänchen shift in synthetic discrete-time heterolattices. *Physical Review Letters, 133*, 083802.
Ranada, A. F. (1989). A topological theory of the electromagnetic field. *Letters in Mathematical Physics, 18*, 97–106.
Ranada, A. F. (1990). Knotted solutions of the Maxwell equations in vacuum. *Journal of Physics A, 23*, L815.
Rodríguez-Lara, B. (2010). Normalization of optical weber waves and weber-gauss beams. *Journal of the Optical Society of America A, 27*, 327–332.
Rubinsztein-Dunlop, H., Forbes, A., Berry, M. V., Dennis, M. R., Andrews, D. L., Mansuripur, M., Denz, C., Alpmann, C., Banzer, P., Bauer, T., et al. (2016). Roadmap on structured light. *Journal of Optics, 19*, 013001.
Saari, P., & Reivelt, K. (1997). Evidence of x-shaped propagation-invariant localized light waves. *Physical Review Letters, 79*, 4135.
Salandrino, A., & Christodoulides, D. N. (2010). Airy plasmon: A nondiffracting surface wave. *Optics Letters, 35*, 2082–2084.
Shen, Y., Hou, Y., Papasimakis, N., & Zheludev, N. I. (2021a). Supertoroidal light pulses as electromagnetic skyrmions propagating in free space. *Nature Communications, 12*, 5891.
Shen, Y., Papasimakis, N., & Zheludev, N. I. (2024a). Nondiffracting supertoroidal pulses and optical "kármán vortex streets". *Nature Communications, 15*, 4863.
Shen, Y., Sun, H., Peng, D., Chen, Y., Cai, Q., Wu, D., ... Ponomarenko, S. A. (2021b). Optical image reconstruction in 4f imaging system: Role of spatial coherence structure engineering. *Applied Physics Letters,* 118.
Shen, Y., Yu, B., Wu, H., Li, C., Zhu, Z., & Zayats, A. V. (2023a). Topological transformation and free-space transport of photonic hopfions. *Advanced Photonics, 5*, 015001.
Shen, Y., Zhan, Q., Wright, L. G., Christodoulides, D. N., Wise, F. W., Willner, A. E., Zou, K.-h., Zhao, Z., Porras, M. A., Chong, A., et al. (2023b). Roadmap on spatiotemporal light fields. *Journal of Optics, 25*, 093001.
Shen, Y., Zhang, Q., Shi, P., Du, L., Yuan, X., & Zayats, A. V. (2024b). Optical skyrmions and other topological quasiparticles of light. *Nature Photonics, 18*, 15–25.
Siegman, A. E. (1986). *Lasers.* University Science Books.
Siviloglou, G. A., Broky, J., Dogariu, A., & Christodoulides, D. (2007). Observation of accelerating airy beams. *Physical Review Letters, 99*, 213901.
Siviloglou, G. A., & Christodoulides, D. N. (2007). Accelerating finite energy airy beams. *Optics Letters, 32*, 979–981.
Starikov, A., & Wolf, E. (1982). Coherent-mode representation of Gaussian schell-model sources and of their radiation fields. *Journal of the Optical Society of America, 72*, 923–928.
Stav, T., Faerman, A., Maguid, E., Oren, D., Kleiner, V., Hasman, E., & Segev, M. (2018). Quantum entanglement of the spin and orbital angular momentum of photons using metamaterials. *Science, 361*, 1101–1104.

Stilgoe, A. B., Nieminen, T. A., & Rubinsztein-Dunlop, H. (2022). Controlled transfer of transverse orbital angular momentum to optically trapped birefringent microparticles. *Nature Photonics, 16*, 346–351.

Sundar, K., Simon, R., & Mukunda, N. (1993). Twisted Gaussian schell-model beams. Ii. spectrum analysis and propagation characteristics. *Journal of the Optical Society of America A, 10*, 2017–2023.

Taddeucci, J., PeñaFernández, J. J., Cigala, V., Kueppers, U., Scarlato, P., DelBello, E., ... Panunzi, S. (2021). Volcanic vortex rings: Axial dynamics, acoustic features, and their link to vent diameter and supersonic jet flow. *Geophysical Research Letters, 48*, e2021GL092899.

Talbot, H. F. (1836). Facts relating to optical science. *Philosophical Magazine, 9*, 401–407.

Urbantke, H. (2003). The hopf fibration—seven times in physics. *Journal of geometry and physics, 46*, 125–150.

Voipio, T., Setälä, T., & Friberg, A. T. (2015). Statistical similarity and complete coherence of electromagnetic fields in time and frequency domains. *Journal of the Optical Society of America A, 32*, 741–750.

Von Kármán, T. (2004). *Aerodynamics: Selected topics in the light of their historical development*. Courier Corporation.

Wan, C., Cao, Q., Chen, J., Chong, A., & Zhan, Q. (2022a). Toroidal vortices of light. *Nature Photonics, 16*, 519–522.

Wan, C., Chen, J., Chong, A., & Zhan, Q. (2022b). Photonic orbital angular momentum with controllable orientation. *National Science Review, 9*, nwab149.

Wan, C., Chong, A., & Zhan, Q. (2023). Optical spatiotemporal vortices. *eLight, 3*, 11.

Wang, F., Chen, Y., Liu, X., Cai, Y., & Ponomarenko, S. A. (2016a). Self-reconstruction of partially coherent light beams scattered by opaque obstacles. *Optics Express, 24*, 23735–23746.

Wang, H., Guo, C., Jin, W., Song, A. Y., & Fan, S. (2021). Engineering arbitrarily oriented spatiotemporal optical vortices using transmission nodal lines. *Optica, 8*, 966–971.

Wang, J., Yang, J.-Y., Fazal, I. M., Ahmed, N., Yan, Y., Huang, H., Ren, Y., Yue, Y., Dolinar, S., Tur, M., et al. (2012). Terabit free-space data transmission employing orbital angular momentum multiplexing. *Nature Photonics, 6*, 488–496.

Wang, T., Comtet, G., LeMoal, E., Dujardin, G., Drezet, A., Huant, S., & Boer-Duchemin, E. (2014). Temporal coherence of propagating surface plasmons. *Optics Letters, 39*, 6679–6682.

Wang, Y., Chen, Y., Zhang, Y., Chen, H., & Yu, S. (2016b). Generalised Hermite–Gaussian beams and mode transformations. *Journal of Optics, 18*, 055001.

Watson, D. W., Jenkins, S. D., Ruostekoski, J., Fedotov, V. A., & Zheludev, N. I. (2016). Toroidal dipole excitations in metamolecules formed by interacting plasmonic nanorods. *Physical Review B, 93*, 125420.

Weiner, A. M. (2011). Ultrafast optical pulse shaping: A tutorial review. *Optics Communications, 284*, 3669–3692.

Wen, J., Zhang, Y., & Xiao, M. (2013). The talbot effect: Recent advances in classical optics, nonlinear optics, and quantum optics. *Advances in Optics and Photonics, 5*, 83–130.

Woltjer, L. (1958). A theorem on force-free magnetic fields. *Proceedings of the National Academy of Sciences, 44*, 489–491.

Xu, Z., Liu, X., Cai, Y., Ponomarenko, S. A., & Liang, C. (2022). Structurally stable beams in the turbulent atmosphere: dark and antidark beams on incoherent background. *Journal of the Optical Society of America A, 39*, C51–C57.

Xu, Z., Liu, X., Chen, Y., Wang, F., Liu, L., Monfared, Y. E., ... Liang, C. (2020). Self-healing properties of hermite-Gaussian correlated schell-model beams. *Optics Express, 28*, 2828–2837.

Yang, S., Ponomarenko, S. A., & Chen, Z. (2015). Coherent pseudo-mode decomposition of a new partially coherent source class. *Optics Letters, 40*, 3081–3084.
Yang, Y., Li, Y., & Wang, C. (2022). Generation and expansion of Laguerre–Gaussian beams. *Journal of Optics, 51*, 910–926.
Yao, A. M., & Padgett, M. J. (2011). Orbital angular momentum: Origins, behavior and applications. *Advances in Optics and Photonics, 3*, 161–204.
Yao, L., Zhang, H., Yuan, Y., Gao, Y., Liang, C., Ponomarenko, S. A., & Cai, Y. (2024). High-fidelity information transmission through the turbulent atmosphere utilizing partially coherent cylindrical vector beams. *Advanced Photonics Research*, 2400137.
Yessenov, M., & Abouraddy, A. F. (2020). Accelerating and decelerating space-time optical wave packets in free space. *Physical Review Letters, 125*, 233901.
Yessenov, M., Allende Motz, A. M., Bhaduri, B., & Abouraddy, A. F. (2021a). Refraction of space-time wave packets: iii. Experiments at oblique incidence. *Journal of the Optical Society of America A, 38*, 1462–1470.
Yessenov, M., Bhaduri, B., & Abouraddy, A. F. (2021b). Refraction of space-time wave packets: I. Theoretical principles. *Journal of the Optical Society of America A, 38*, 1409–1422.
Yessenov, M., Bhaduri, B., Kondakci, H. E., Meem, M., Menon, R., & Abouraddy, A. F. (2019a). Non-diffracting broadband incoherent space–time fields. *Optica, 6*, 598–607.
Yessenov, M., Free, J., Chen, Z., Johnson, E. G., Lavery, M. P., Alonso, M. A., & Abouraddy, A. F. (2022a). Space-time wave packets localized in all dimensions. *Nature Communications, 13*, 4573.
Yessenov, M., Hall, L. A., Ponomarenko, S. A., & Abouraddy, A. F. (2020). Veiled talbot effect. *Physical Review Letters, 125*, 243901.
Yessenov, M., Hall, L. A., Schepler, K. L., & Abouraddy, A. F. (2022b). Space-time wave packets. *Advances in Optics and Photonics, 14*, 455–570.
Yessenov, M., Mach, L., Bhaduri, B., Mardani, D., Kondakci, H. E., Atia, G. K., ... Abouraddy, A. F. (2019b). What is the maximum differential group delay achievable by a space-time wave packet in free space? *Optics Express, 27*, 12443–12457.
Zang, Y., Mirando, A., & Chong, A. (2022). Spatiotemporal optical vortices with arbitrary orbital angular momentum orientation by astigmatic mode converters. *Nanophotonics, 11*, 745–752.
Zauderer, E. (1986). Complex argument Hermite–Gaussian and laguerre–Gaussian beams. *Journal of the Optical Society of America A, 3*, 465–469.
Zayats, A. V., Smolyaninov, I. I., & Maradudin, A. A. (2005). Nano-optics of surface plasmon polaritons. *Physics Reports, 408*, 131–314.
Zhan, Q. (2024). Spatiotemporal sculpturing of light: A tutorial. *Advances in Optics and Photonics, 16*, 163–228.
Zhang, J., Zhang, L., & Xu, W. (2012). Surface plasmon polaritons: Physics and applications. *Journal of Physics D: Applied Physics, 45*, 113001.
Zhang, Y., Cao, Q., Chong, A., & Zhan, Q. (2025). Full space-time talbot effect. *Optics Express, 33*, 12147–12155.
Zhu, X., Wang, F., Zhao, C., Cai, Y., & Ponomarenko, S. A. (2019). Experimental realization of dark and antidark diffraction-free beams. *Optics Letters, 44*, 2260–2263.
Ziolkowski, R. W. (1989). Localized transmission of electromagnetic energy. *Physical Review A, 39*, 2005.

This page intentionally left blank